Nonlinear Identification through eXtended Outputs (NIXO) with Numerical and Experimental Validation using Geometrically Nonlinear Structures

Michael Kwarta[1] and Matthew S. Allen[2]

[1] University of Wisconsin - Madison, Mechanical Engineering Department
1500 Engineering Drive, Engineering Research Building, Madison, WI 53706, USA
Email address: kwarta@wisc.edu

[2] Brigham Young University, Mechanical Engineering Department
350B Engineering Building, Provo, UT 84602, USA
Email address: matt.allen@byu.edu

Abstract

This work presents a novel technique for nonlinear system identification that operates in the frequency domain and fits a model to measured spectra to estimate the parameters in a modal domain nonlinear equation of motion (EOM). Nonlinear terms are added to the linear EOM in the form of polynomials, and the proposed algorithm estimates the polynomial coefficients as well as the underlying linear Frequency Response Function (FRF). This method is an extension to a popular nonlinear system identification algorithm called NIFO, from Nonlinear Identification through Feedback of the Outputs. However, NIFO identifies the nonlinear parameters as complex numbers that may be different at each frequency line, even though the mechanical system is expected to be governed by an EOM in which the nonlinear parameters are real and constant with frequency. This might be problematic, because any variation in the identified nonlinear parameters will distort the linear FRFs estimated by NIFO, and those linear FRFs are important to tell the user whether all of the significant nonlinearity has been extracted from the system. The proposed algorithm, here dubbed Nonlinear Identification through eXtended Outputs (NIXO), estimates the nonlinear parameters as frequency-independent and real. Additionally, it is demonstrated that for the systems studied here that the algorithm works when random and swept-sine inputs are used to excite the tested structure, while NIFO only worked well when random inputs were used. The method is first evaluated numerically using benchmark case studies, starting with the SDOF equation and then reduced models of a clamped-clamped flat beam, and the results are compared to those obtained with NIFO. Then the algorithm is applied to swept-sine measurements from a 3D-printed flat beam and the results are validated by computing the primary nonlinear normal mode of the identified model and comparing it with measurements.

Keywords: Nonlinear System Identification, NIFO, Nonlinear Parameter Estimation, Nonlinear Experimental Dynamics, Geometrically Nonlinear Structures, Swept-Sine and Burst-Random Vibration Testing

Contents

1 Introduction

System identification plays a significant role in engineering design process, helping in correlating numerical or mathematical models with the actual real-life structures. Once the virtual representation of a mechanical system is found, it can be further used in: *(i)* predicting the structure's motion or *(ii)* redesigning or optimizing the structure. Many system identification methods are available and have found success in identifying certain linear and/or nonlinear systems. However, there are many cases in which existing algorithms are still not successful in identifying an accurate model from measurements. Much work is still needed in this field to develop a toolbox of methods that can give adequate results when applied to any system, just as linear system identification can handle almost any linear system.

When it comes to *linear* system ID, one of the most popular ways to identify these type of structures is, so called, *modal parameter estimation*. The objective there is to extract the linear natural frequencies, damping ratios and mode shapes [1, 2]. However, many mechanical systems exhibit nonlinear behavior when oscillating at modest amplitudes; for example the bolted assemblies that are ubiquitous in industry often exhibit nonlinearity due to micro-slip. Moreover, demand for lighter yet more durable structures has encouraged the scientific community to pursue design and testing methods for structures that have intentional nonlinearities. For example, geometric nonlinearities can be designed to limit resonant amplitudes and hence the stresses that a structure experiences.

Following Kerschen et al. [3], the nonlinear system identification procedure can be divided into three stages: detection, characterization and parameter estimation. In the first stage, one checks whether a nonlinearity is simply present in the system or not. Then, the source and type of the nonlinearity can be determined. One can then postulate a mathematical model to capture the nonlinear behavior. Finally, in the parameter estimation step the values of the unknown coefficients in the model are found. The algorithm presented in this work addresses the last of these stages.

Naturally, there are different kinds of the nonlinear system ID methods. In [4], Noël and Kerschen used various classifications, with time- and frequency-domain being one important distinction, although

even in that case the lines can become blurred as the input data can be transferred to the frequency domain via a Fourier transform. However, the vast majority of nonlinear system identification techniques share one feature in common, they treat the nonlinearities as auxiliary inputs that are known because the nonlinearities are assumed to be known functions of the measured outputs. The algorithm proposed here falls in this class. The following section reviews some of the most common methods that can also be classified in this category, as well as some newer, emerging techniques and contrasts them with the proposed approach.

Before proceeding, it is worth mentioning a few methods that do not belong to this category. *(i)* The most common nonlinear system identification techniques are those brute-force methods that simply integrate the equation of motion (EOM), compare it with measurements, and iterate on the model parameters to bring the two into agreement. They are generally accepted to be inefficient and often unlikely to converge to a local minimum, although they have proven effective in some cases. *(ii)* Time-frequency methods such as the Hilbert transform [5] assume that the response at any instant can be approximated by a linear system, but the parameters of that linear system are allowed to evolve with time or as the amplitude of vibration changes. One example is the FORCED-VIB method by Feldman [6] and the extension by Moldenhauer et al. [7] in which the system was assumed to be linear but with coefficients that are smooth polynomial functions of time. This class of methods has been extremely successful in treating systems with weak nonlinearities. For example, in [7] the authors identified a model of a single degree of freedom (SDOF) system with a nonlinear, hysteretic Iwan element [8, 9] as well as the continuous, multi-degree-of-freedom cylinder-plate-beam benchmark structure [10]. Finally, *(iii)* methods based on higher order frequency response functions (FRFs) [11, 12] or Volterra series [13], while not used too often, could be argued to provide non-parametric identification in the frequency domain. Some additional methods are elaborated in [4].

Additionally, in the past decade various methods have emerged that directly identify the nonlinear normal modes (NNMs) of a system, for example control based continuation (CBC) or phase locked loop (PLL) [14–19]. This type of identification may at first seem to be in a different class, as rather than identifying a differential equation governing the system, it produces the nonlinear modes, which are special solutions to the differential equation. However, recent works in this area [20, 21] have shown that this type of approach can produce a model that can be used to predict the near-resonant response and not just the NNMs. These methods have proven powerful and efficient and have obtained excellent results on structures with geometric nonlinearity such as the ones studied here (e.g. see [20,21]). In fact, the authors proposed one such method in [22] and applied it to the geometrically nonlinear structures presented in this work. However, it is important to note that these methods require that the inputs to the system be modified in real time to drive the system to a desired condition, i.e. resonance for CPC or PLL or to a specified amplitude using RCT method (from Response-Controlled Stepped-Sine Testing) in [20, 21]. This work focuses on methods in which the input and output signals are broadband and acquired in open loop, and so these methods will not be considered further here.

1.1 Time- and Frequency-Domain System ID Methods

Most nonlinear system identification methods make use of the idea of nonlinear feedback, in which the system is treated as linear but with nonlinear outputs treated as additional input forces. If the form of the nonlinear force is known, i.e suppose $f_{nl} = Cx^2$ where C is a constant and x is the measured output, then the force f_{nl} may be treated as an input with an unknown scale factor and a least squares procedure used to identify the scale factor.

The Restoring Force Surface (RFS) method, introduced in 1979 [23], is the most basic of these approaches. For a single degree of freedom system, the measured response is integrated and/or differentiated so that acceleration, velocity and displacement are known, and then one can plot the unknown nonlinear force as a surface in the displacement-velocity plane and determine the nature of the nonlinearity. For

higher order systems one must know the form of the nonlinearity, but if that is known then one can formulate a least squares problem to find the coefficients on the nonlinear forces. The reader can refer to [24] and [25] for examples where RFS was applied to mechanical systems exhibiting softening-stiffening and pure stiffening characteristics respectively. A variation on the RFS method, proposed by Aykan and Özgüven, can be found in [26]. Moldenhauer et al. [27] generalized the approach by allowing the polynomial nonlinearities to have non-integer exponents, and while this improved the results for a hysteretic system relative to the original RFS, none of the identified models was able to reproduce the response adequately when subjected to the measured input forces.

One of the most significant challenges encountered when using this method is to accurately differentiate or integrate the vibration measurements. By extension, that same difficulty is present for all continuous-time methods that are based on the nonlinear feedback concept. That challenge is different at least if one instead operates in the discrete-time domain. Perhaps the most common algorithm of this class is NARMAX, from Nonlinear AutoRegressive Moving Average with eXogenous inputs [28, 29]. It has proven to be successful in identifying various types of nonlinear systems. The Time-Domain Nonlinear Subspace Identification (TNSI) methods [30, 31] are another example of such an approach. In both cases, the nonlinearities become polynomial functions of the response at past time steps, rather than polynomial functions of the response and its integral or derivative.

Several methods have sought to operate in the frequency domain rather than the time domain. This is mainly because the features in the data are more apparent there, and this also allows one to easily exclude frequency ranges where the response is noisy or contaminated.

The Conditioned Reverse Path (CRP) [32] and Nonlinear Identification through Feedback of the Outputs (NIFO) methods are well-known *frequency*-domain algorithms, both of which are again based on the extended input concept. NIFO was first presented by Adams and Allemang [33] as a $\mathbf{H}_1$-based estimator and later an $\mathbf{H}_2$ version was developed by Haroon and Adams [34]. The term "$\mathbf{H}$" stands for the linear part of the system being estimated in the form of the frequency response function, while subscripts "1" and "2" denote whether the inputs or outputs are used to form the cross spectra used in the NIFO method (analogous to the well-known $\mathbf{H}_1$ and $\mathbf{H}_2$ linear estimators). Perhaps the most advantageous feature of these methods is the fact that, if all of the nonlinear terms can be extracted, then the methods return the linear frequency response functions. If the nonlinearity is correctly identified, then the linear FRFs should converge to the expected shapes and not contain any nonlinear distortions. This provides a valuable check on the methods. The methods are also computationally efficient because a large quantity of data can be condensed into relatively compact cross-spectra. The CRP method was sucessfully applied to both numerical and experimental nonlinear systems in [35] and [36] and NIFO was successfully applied to a flat steel beam in [37]. However, in other cases the CRP method does not prove satisfactory, for example in [38] where there were many nonlinear parameters to identify. In particular, the NIFO and CRP methods treat each frequency line as independent, hence they identify nonlinear coefficients that are complex and can vary with frequency. These must be averaged over frequency to obtain physically meaningful values. Moreover, these methods work only when the nonlinear equation governing the dynamics of the system is guessed correctly. Otherwise, the nonlinearity present in the structure's response is not entirely filtered out during the identification process and can affect the estimate of the linear FRF shape. Additionally, the linear FRFs approximated by these methods are only valid for a nonlinear system with frequency-varying nonlinear parameters, and hence they become misleading if the frequency variation is significant.

One promising alternative to these methods is the Frequency-Domain Nonlinear Subspace Identification (FNSI) [36] method. While it is also based on the same nonlinear feedback concept, it formulates the discrete time equations of motion in the frequency domain, allowing the algorithm to only need measurements at frequencies near resonance, thus improving the computational efficiency significantly as compared to the time-domain subspace methods. The identified nonlinear coefficients are complex numbers, and when they are transferred back to the continuous-time domain they become frequency varying. However, in the applications in [36] both the imaginary parts and the variations with frequency

were practically negligible and far better than those identified by the CRP method. Even then, in other cases it can prove more difficult to obtain parameters that are relatively constant with frequency and hence physically reasonable, even with this advanced algorithm [18].

1.2 Objectives and Contributions

This article proposes a novel algorithm called NIXO (for *Nonlinear Identification through eXtended Outputs*), which is an extension to NIFO/CRP since it forces the nonlinear parameters to be real and constant with frequency. The identification process with NIXO can be divided into three steps. In the first one, the user must postulate an equation of motion describing the nonlinear structure. Then, the input and output signals (collected in the experimental tests) are provided to NIXO and used to compute various auto- and cross-spectra. In the final step, a least squares problem is solved to obtain the values of the parameters. Once a model for the system has been identified, it is often helpful to validate the results, for example by computing the nonlinear normal mode(s) of the system and overlaying them with swept sine measurements.

This work builds on that in [33] and [34] where Adams, Haroon et al. proposed the $\mathbf{H}_1$- and $\mathbf{H}_2$-based NIFO algorithms, respectively. NIFO identifies structures via solving many relatively small sets of equations, each corresponding to a different frequency line. The proposed NIXO algorithm creates one large linear system of equations and solves it to obtain the underlying linear system representation at all frequencies as well as a single estimate for each nonlinear coefficient, which is real and not a function of frequency. Analogous to NIFO, two variations of NIXO are presented. Namely, the $\mathbf{D}_1$- and $\mathbf{D}_2$-based NIXO. The term "$\mathbf{D}$" stands for the dynamic stiffness, since NIXO estimates the linear part of the mechanical system in such form (whereas NIFO estimates the FRF directly). Subscripts "1" and "2" still indicate whether the cross spectra are obtained via right-multiplying the equations of motion with the inputs or outputs, respectively. While the derivation of NIXO is similar to that of the NIFO algorithm, there are some important differences and few options are encountered that are addressed in the derivation.

The proposed NIXO method is also demonstrated both numerically and experimentally and the results are compared against those obtained using the popular NIFO methods. The algorithms are first evaluated numerically using benchmark single degree of freedom (SDOF) systems. Then, they are employed to identify reduced models for two flat beams. The first using the numerical data generated using an ICE-ROM of a beam (which is a reduced order model supported by the implicit condensation and expansion method [39, 40]), while the second uses experimental measurements collected on an actual, 3D printed beam to identify a model. In these case studies, two different types of forcing signals are used: swept sines and burst random signals.

Section 2, presents a derivation of the proposed NIXO algorithm and discusses how the results can be validated. In Section 3, the NIXO and NIFO methods are evaluated using simulated measurements from benchmark SDOF systems. In Section 4, the techniques are further employed numerically by applying them to ICE-ROM of a flat beam, and the outcomes are validated and discussed. Section 5 shows the results using experimental measurements from a flat beam that was 3D-printed in polymer (polylactide acid). Finally, Section 6 presents conclusions and future work.

2 Derivation of the NIXO Algorithms

The derivation starts with the steps common for all the algorithms presented in this work, and each separate method is addressed. Consider a multi-degree-of-freedom (MDOF) nonlinear mechanical system, with linear viscous damping, described with equation of motion defined in (1).

$$\mathbf{M}\ddot{\mathbf{x}} + \mathbf{C}\dot{\mathbf{x}} + \mathbf{K}\mathbf{x} + \mathbf{f}_{nl}(\mathbf{x}, \dot{\mathbf{x}}) = \mathbf{f}(t), \tag{1}$$

where $\mathbf{M}$, $\mathbf{C}$ and $\mathbf{K}$ are square matrices modeling mass, linear damping and stiffness distributions present in the system. Vector $\mathbf{f}(t)$ represents the force distribution applied to the structure, while $\mathbf{x}(t)$ is its

displacement response. Finally, $\mathbf{f}_{nl}(\mathbf{x}, \dot{\mathbf{x}})$ is the nonlinear restoring force that is a function of the displacement and velocity terms.

Using the well-known modal transformation (2), the dynamics of the nonlinear system can be expressed in the modal domain, as shown in (3).

$$\mathbf{x} = \mathbf{\Phi}\mathbf{q} \tag{2}$$

$$\ddot{\mathbf{q}} + \begin{bmatrix} 2\zeta_1\omega_1 & & \\ & \ddots & \\ & & 2\zeta_{N_{lin}}\omega_{N_{lin}} \end{bmatrix} \dot{\mathbf{q}} + \begin{bmatrix} \omega_1^2 & & \\ & \ddots & \\ & & \omega_{N_{lin}}^2 \end{bmatrix} \mathbf{q} + \boldsymbol{\theta}_{nl}(\mathbf{q}, \dot{\mathbf{q}}) = \mathbf{\Phi}^T \mathbf{f}(t), \tag{3}$$

where: ω_k and ζ_k are, respectively, the natural frequency and damping ratio of the k-th linear mode, the columns of matrix $\mathbf{\Phi}$ are the the mass-normalized eigen-shapes of the linearized, undamped and homogeneous equation of motion (1), $\boldsymbol{\theta}_{nl}(\mathbf{q}, \dot{\mathbf{q}})$ are the nonlinear forces transformed into the modal domain (or $\boldsymbol{\theta}_{nl}(\mathbf{q}, \dot{\mathbf{q}}) = \mathbf{\Phi}^T \mathbf{f}_{nl}(\mathbf{\Phi}^\dagger \mathbf{x}, \mathbf{\Phi}^\dagger \dot{\mathbf{x}})$, where $(\dagger)$ represents the pseudo-inverse matrix operator), and N_{lin} stands for the number of linear modes taken into consideration. The linear damping is assumed to be diagonalized by the modes, i.e. classical damping is assumed. However, the modal EOM in Eq. (3) are coupled via the nonlinear terms $\theta_{nl,k}(\mathbf{q}, \dot{\mathbf{q}})$, as indicated in Eqs. (4–6), and one could presumably add terms to account for coupling due to the linear damping.

$$\ddot{q}_k + 2\zeta_k\omega_k\dot{q}_k + \omega_k^2 q_k + \theta_{nl,k}(\mathbf{q}, \dot{\mathbf{q}}) = \psi_k(t), \tag{4}$$

where:

$$\psi_k(t) = \mathbf{\Phi}_k^T \mathbf{f}(t) \tag{5}$$

and

$$\begin{aligned} \theta_{nl,k}(\mathbf{q}, \dot{\mathbf{q}}) = \mathbf{\Phi}_k^T \mathbf{f}_{nl}(\mathbf{\Phi}^\dagger \mathbf{x}, \mathbf{\Phi}^\dagger \dot{\mathbf{x}}) \triangleq \alpha_{11}^{v,k}\dot{q}_1^2 + \alpha_{12}^{v,k}\dot{q}_1\dot{q}_2 + \cdots + \alpha_{11}^{k} q_1^2 + \alpha_{12}^{k} q_1 q_2 + \cdots + \\ + \beta_{111}^{v,k}\dot{q}_1^3 + \beta_{112}^{v,k}\dot{q}_1^2\dot{q}_2 + \cdots + \beta_{111}^{k} q_1^3 + \beta_{112}^{k} q_1^2 q_2 + \ldots \end{aligned} \tag{6}$$

Equation (6) expresses the $\theta_{nl,k}(\mathbf{q}, \dot{\mathbf{q}})$ function in a polynomial form including squared and cubed terms, which is a popular way to model the response of the *geometrically nonlinear* structures with material assumed to be linear elastic. However, sometimes including higher order terms might also be necessary, for example when a structure exhibits an unstable snap-through behaviors (as presented in [41]), or even more sophisticated terms in order to capture phenomena going beyond geometric nonlinearities [42, 43]. The subscripts of the nonlinear parameters correspond to the product of polynomial terms they multiply; for example: β_{111} multiplies term q_1^3, while β_{123} – term $q_1 q_2 q_3$. In most cases one will not require all of the terms in Eq. (6) for a particular system. As a result, in this article a more general form, shown in Eq. (7), is used.

$$\theta_{nl,k}(\mathbf{q}, \dot{\mathbf{q}}) \triangleq \gamma_1^{v,k} p_1^v + \gamma_2^{v,k} p_2^v + \cdots + \gamma_1^k p_1 + \gamma_2^k p_2 + \ldots \ , \tag{7}$$

where $\gamma_r^v p_r^v$ and $\gamma_r p_r$ stand for the r-th nonlinear damping and stiffness terms, respectively. Functions p_r^v and p_r are the products of the modal coordinates' time representations of the users choice. To clarify, if the nonlinear stiffness of the structure can be modeled with $q_1^3(t)$ and $q_1(t)q_2(t)q_3(t)$ terms only, then $p_1(t) = q_1^3(t)$ and $p_2(t) = q_1(t)q_2(t)q_3(t)$.

It is worth noting that, while this work focuses on geometrically nonlinear structures, or systems with distributed nonlinearities that are more easily addressed in the modal domain, the algorithm is potentially applicable to systems with localized nonlinearities. As shown above, a localized nonlinearity can be expressed as a polynomial nonlinearity in the modal domain, typically including coupling terms

between the modes, and hence can be identified using the approach presented here. Such an approach may or may not be desirable, as one localized nonlinearity can lead to many terms in the modal domain and many localized nonlinearities may produce only a single unique term in the modal domain; these issues are left for a future work.

Using a Fourier series, the time functions defined above can be decomposed into sums of harmonically related sinusoids, as presented in Eq. (8).

$$q_k(t) = \mathrm{Re}\left\{\sum_{s=0}^{n} Q_k^s \; e^{is\Omega_1 t}\right\} \tag{8a}$$

$$\psi_k(t) = \mathrm{Re}\left\{\sum_{s=0}^{n} \Psi_k^s \; e^{is\Omega_1 t}\right\} \tag{8b}$$

$$p_r^v(t) = \mathrm{Re}\left\{\sum_{s=0}^{n} P_r^{v,s} \; e^{is\Omega_1 t}\right\} \forall_r \tag{8c}$$

$$p_r(t) = \mathrm{Re}\left\{\sum_{s=0}^{n} P_r^{s} \; e^{is\Omega_1 t}\right\} \forall_r \tag{8d}$$

Each complex amplitude Q_k^s, Ψ_k^s, $P_r^{v,s}$ and P_r^s corresponds to the s-th frequency sample $s\Omega_1$, where Ω_1 is the fundamental frequency in the Fourier series, and n is the total number of frequency samples. Now, the equation of motion of the k-th mode can be expressed in the frequency domain, as presented in Eq. (9).

$$D_k(\Omega)\; Q_k(\Omega) + \gamma_1^{v,k}\; P_1^v(\Omega) + \cdots + \gamma_1^k\; P_1(\Omega) + \cdots = \Psi_k(\Omega), \tag{9}$$

where $\Omega = s\Omega_1$, and $D_k(\Omega)$ is a dynamic stiffness defined in Eq. (10). The dynamic stiffness is the reciprocal of the frequency response function (FRF), $H_k(\Omega)$, whose explicit mathematical form is provided in Eq. (11). Note that by writing the equations of motion in the modal domain, the relationship between the dynamic stiffness and the frequency response becomes merely a reciprocal relationship rather than a matrix inverse.

$$D_k(\Omega) = \omega_k^2 - \Omega^2 + 2i\zeta_k\omega_k\Omega \tag{10}$$

$$H_k(\Omega) = \frac{1}{D_k(\Omega)} = \frac{1}{\omega_k^2 - \Omega^2 + 2i\zeta_k\omega_k\Omega} \tag{11}$$

The equations above assume that the signals are obtained by taking the FFT of a single time signal, when in practice it proves beneficial to break each time signal $q_k(t)$, $p_r^v(t)$, $p_r(t)$, and $\psi_k(t)$, into several overlapping pieces and applying a window (e.g. the Hann window) to each signal. Then, Eq. (11) can be written in a matrix form where matrices $\mathbf{Q}_k$, $\mathbf{P}_r^v$, $\mathbf{P}_r$, and $\mathbf{\Psi}_k$ in Eqs. (12a) and (12b) have size of $1 \times N_{avg}$, where N_{avg} is the number of blocks that the time signals have been split into. Additionally, Eqs. (12a) and (12b) can be written for each frequency, $s \in \{0, \ldots, n\}$.

$$D_k(\Omega)\; [Q_{k,1},\; \ldots,\; Q_{k,N_{avg}}] + \gamma_1^{v,k}\; [P_{1,1}^v,\; \ldots,\; P_{1,N_{avg}}^v] + \cdots + \gamma_1^k\; [P_{1,1},\; \ldots,\; P_{1,N_{avg}}] + \ldots = [\Psi_{k,1},\; \ldots,\; \Psi_{k,N_{avg}}] \tag{12a}$$

$$D_k(\Omega)\; \mathbf{Q}_k(\Omega) + \gamma_1^{v,k}\; \mathbf{P}_1^v(\Omega) + \cdots + \gamma_1^k\; \mathbf{P}_1(\Omega) + \ldots = \mathbf{\Psi}_k(\Omega) \tag{12b}$$

2.1 NIXO Algorithms

2.1.1 $\mathbf{D}_1$–based NIXO for ROMs

To derive the $\mathbf{D}_1$-based NIXO estimator, we post-multiply Eq. (12b) by $\mathbf{\Psi}_k^H$ (which is the Hermitian or conjugate transpose of $\mathbf{\Psi}_k$) to obtain Eq. (13).

$$D_k(\Omega)\ \mathbf{Q}_k\mathbf{\Psi}_k^H + \gamma_1^v\ \mathbf{P}_1^k\mathbf{\Psi}_k^H + \cdots + \gamma_1\ \mathbf{P}_1^k\mathbf{\Psi}_k^H + \cdots = \mathbf{\Psi}_k\mathbf{\Psi}_k^H \tag{13}$$

The term $\mathbf{Q}_k\mathbf{\Psi}_k^H$ is merely a sum over all of the windowed time blocks as shown in Eq. (14) and (if divided by N_{avg}) it becomes an estimate for a power spectrum $S_{Q\Psi}$ (also shown in Eq. (14)) between the signals Q_k and Ψ_k. Power spectra $S_{P_1^v\Psi},\ \ldots,\ S_{P_1\Psi},\ \ldots, S_{\Psi\Psi}$ are obtained in the same manner.

$$\frac{1}{N_{avg}}\mathbf{Q}_k\mathbf{\Psi}_k^H = \frac{1}{N_{avg}}\left(\sum_{i=1}^{N_{avg}} Q_{k,i}\Psi_{k,i}^H\right) = S_{Q\Psi} \tag{14}$$

Hence, dividing both sides of Eq. (13) by N_{avg} we obtain Eq. (15).

$$D_k(\Omega)\ S_{Q\Psi}\ + \gamma_1^v\ S_{P_1^v\Psi}\ + \cdots + \gamma_1\ S_{P_1\Psi}\ + \cdots =\ S_{\Psi\Psi} \tag{15}$$

Note that Eq. (15) is valid for every individual frequency line. The NIFO and CRP algorithms solve an equation that is similar to this individually for each frequency line, and hence the estimates for the nonlinear parameters that they obtain vary with frequency. However, knowing that the nonlinear parameters are independent of frequency, one can collect the equations for all frequency lines and obtain the matrix form presented in Eq. (16). The frequency sample number is indicated in the quantities' sub- or superscripts, e.g. $S_{Q\Psi}(\Omega_s) = S_{Q\Psi}^s$ or $D_k(\Omega_s) = D_k^s$ and n stands for the number of frequency samples.

$$\underbrace{\begin{bmatrix} S_{Q\Psi}^0 & & & S_{P_1^v\Psi}^0 & & S_{P_1\Psi}^0 & \\ & \ddots & & \vdots & \cdots & \vdots & \cdots \\ & & S_{Q\Psi}^n & S_{P_1^v\Psi}^n & & S_{P_1\Psi}^n & \end{bmatrix}}_{\mathbf{S}_{D1}^{cross}} \begin{bmatrix} D_k^0 \\ \vdots \\ D_k^n \\ \gamma_1^v \\ \vdots \\ \gamma_1 \\ \vdots \end{bmatrix} = \underbrace{\begin{bmatrix} S_{\Psi\Psi}^0 \\ \vdots \\ S_{\Psi\Psi}^n \end{bmatrix}}_{\mathbf{S}_{D1}^{auto}}, \tag{16}$$

This equation forms the basis of the proposed algorithm, which is called the ***$\mathbf{D}_1$-based Nonlinear Identification through eXtended Outputs*** ($\mathbf{D}_1$-based NIXO). However, Eq. (16) cannot be solved by inverting the matrix on the left, because this system of linear equations is underdetermined. To be more precise, the numbers of equations and unknowns are, respectively, $2n+1$ and $2n+2+p_{damp}+p_{stiff}$ (since some of the parameters in Eq. (16) are complex numbers in general). Quantities p_{damp} and p_{stiff} represent the number of the nonlinear damping and stiffness terms in Eq. (16), respectively. This indeterminacy is addressed by applying at least two distinct inputs to the system and including the input and output data sets in Eq. (16), so that the number of rows is at least doubled. This assumes that the system parameters in Eqs. (4) and (7), namely $\omega_k,\ \zeta_k,\ \gamma_s^v$ and γ_s, are independent of the excitation type or time. Hence, the $(2n+2+p_{damp}+p_{stiff})$ unknowns in Eq. (16) are exactly the same for each vibration test. Furthermore, measurements are used where the nonlinear structure is oscillating at, say, two different amplitudes, then it is more likely that the equations will be linearly independent.

In order to clarify this and a few additional issues, this concept is defined mathematically below. Consider the the equation for a single mode k, subjected to various forcing functions in multiple different tests (e.g. they could be multiple swept sines of different forcing levels). Each response is the solution to one of the differential equations in Eq. (17).

$$\begin{cases} \ddot{q}_k + 2\zeta_k\omega_k\dot{q}_k + \omega_k^2 q + \theta_{nl,k}(\mathbf{q},\dot{\mathbf{q}}) &= \psi_{k,I}(t) \\ \ddot{q}_k + 2\zeta_k\omega_k\dot{q}_k + \omega_k^2 q + \theta_{nl,k}(\mathbf{q},\dot{\mathbf{q}}) &= \psi_{k,II}(t) \\ & \vdots \\ \ddot{q}_k + 2\zeta_k\omega_k\dot{q}_k + \omega_k^2 q + \theta_{nl,k}(\mathbf{q},\dot{\mathbf{q}}) &= \psi_{k,r}(t) \end{cases}, \tag{17}$$

where r is the number of different forcing functions used to excite the mechanical system. Now, if the derivation presented above is repeated for the equations of motion (17), one would end up with r-times the number of equations presented in (16) and an unchanged number of unknowns, with the final form given in Eq. (18).

$$\begin{bmatrix} \mathbf{S}_{D1,I}^{cross} \\ \mathbf{S}_{D1,II}^{cross} \\ \vdots \\ \mathbf{S}_{D1,r}^{cross} \end{bmatrix} \begin{bmatrix} D_k^0 \\ \vdots \\ D_k^n \\ \gamma_1^v \\ \vdots \\ \gamma_1 \\ \vdots \end{bmatrix} = \begin{bmatrix} \mathbf{S}_{D1,I}^{auto} \\ \mathbf{S}_{D1,II}^{auto} \\ \vdots \\ \mathbf{S}_{D1,r}^{auto} \end{bmatrix} \tag{18}$$

Since some of the parameters in Eq. (18) are complex, the estimates of γ_j^v's and γ_j's are not guaranteed to be real numbers. To overcome this issue, the real and imaginary parts of the unknowns should be estimated separately, so that the nonlinear parameters are forced to be real. To do so, Eq. (18) is broken into real and imaginary parts as presented in Eq. (19). The $\boldsymbol{\sigma}_{D1}^{cross}$ and $\boldsymbol{\sigma}_{D1}^{auto}$ matrices computed using a data measured in a single vibration test are defined in (20) and (21), respectively. The system of derived equations, Eqs. (19), is overdetermined and the unknown parameters can be estimated by solving a linear least squares problem.

$$\begin{bmatrix} \boldsymbol{\sigma}_{D1,I}^{cross} \\ \boldsymbol{\sigma}_{D1,II}^{cross} \\ \vdots \\ \boldsymbol{\sigma}_{D1,r}^{cross} \end{bmatrix} \begin{bmatrix} D_k^0 \\ \vdots \\ D_k^n \\ \gamma_1^v \\ \vdots \\ \gamma_1 \\ \vdots \end{bmatrix} = \begin{bmatrix} \boldsymbol{\sigma}_{D1,I}^{auto} \\ \boldsymbol{\sigma}_{D1,II}^{auto} \\ \vdots \\ \boldsymbol{\sigma}_{D1,r}^{auto} \end{bmatrix} \tag{19}$$

$$\boldsymbol{\sigma}_{D1}^{cross} = \begin{bmatrix} Re\{S_{Q\Psi}^0\} & -Im\{S_{Q\Psi}^0\} & & & & & Re\{S_{P_1^v\Psi}^0\} & & Re\{S_{P_1\Psi}^0\} & \\ Im\{S_{Q\Psi}^0\} & Re\{S_{Q\Psi}^0\} & & & & & Im\{S_{P_1^v\Psi}^0\} & & Im\{S_{P_1\Psi}^0\} & \\ & & \ddots & & & & \vdots & \cdots & \vdots & \cdots \\ & & & Re\{S_{Q\Psi}^n\} & -Im\{S_{Q\Psi}^n\} & & Re\{S_{P_1^v\Psi}^n\} & & Re\{S_{P_1\Psi}^n\} & \\ & & & Im\{S_{Q\Psi}^n\} & Re\{S_{Q\Psi}^n\} & & Im\{S_{P_1^v\Psi}^n\} & & Im\{S_{P_1\Psi}^n\} & \end{bmatrix} \tag{20}$$

$$\boldsymbol{\sigma}_{D1}^{auto} = \begin{bmatrix} Re\{S_{\Psi\Psi}^0\} \\ Im\{S_{\Psi\Psi}^0\} \\ \vdots \\ Re\{S_{\Psi\Psi}^n\} \\ Im\{S_{\Psi\Psi}^n\} \end{bmatrix} \tag{21}$$

Notice that the system of equations (19) is far larger than those used for NIFO (see [33,34], or Appendix A for their derivation). In NIFO one would have to solve multiple systems of equations with only a few unknown parameters in each of them, whereas $\left[D_k^0,\ \ldots,\ D_k^n\right]$ is a vector of the frequency response, typically with thousands of lines. However, with today's computers this does not pose serious challenge.

2.1.2 $\mathbf{D}_2$–based NIXO for ROMs

The derivation of the $\mathbf{D}_1$-based NIXO algorithm in the previous section started by post-multiplying the equation of motion (12b) with the hermitian transpose of the input spectra $\mathbf{\Psi}^H$, resulting in Eq. (13). This post multiplication by the spectrum of the forces is akin to what is done in the commonly used linear $\mathbf{H}_1$ estimator. Similarly, to obtain the $\mathbf{D}_2$-NIXO estimator, Eq. (12b) is post-multiplied by the conjugate transpose of the output signal(s). However, because the set of output signals could also include the nonlinear functions of the response, several different versions of this algorithm can be derived, as illustrated in Eq. (22).

$$\left(D_k(\Omega)\ \mathbf{Q}_k + \gamma_1^v\ \mathbf{P}_1^{v,k} + \cdots + \gamma_1\ \mathbf{P}_1^k + \cdots = \mathbf{\Psi}_k\right)\mathbf{Q}_k^H \tag{22a}$$

$$\left(D_k(\Omega)\ \mathbf{Q}_k + \gamma_1^v\ \mathbf{P}_1^{v,k} + \cdots + \gamma_1\ \mathbf{P}_1^k + \cdots = \mathbf{\Psi}_k\right)\left[\mathbf{Q}_k^H \quad (\mathbf{P}_s^k)^H\right] \tag{22b}$$

$$\left(D_k(\Omega)\ \mathbf{Q}_k + \gamma_1^v\ \mathbf{P}_1^{v,k} + \cdots + \gamma_1\ \mathbf{P}_1^k + \cdots = \mathbf{\Psi}_k\right)\left[\mathbf{Q}_k^H \quad (\mathbf{P}_1^{v,k})^H \quad \ldots \quad (\mathbf{P}_1^k)^H \quad \ldots\right] \tag{22c}$$

The case studies presented in this work use the first of these, or the $\mathbf{D}_2$–NIXO estimator obtained when the EOM (12b) are multiplied by *the linear output spectra only* (see Eq. (22a)). Hence, this section presents the derivation for this estimator. One of the alternatives can be obtained when *all the outputs* are used to right-multiply the EOM (see Eq. (22c)). Its derivation can be found in the extended version of this article [44].

Expanding the product in Eq. (22a) produces Eq. (23), which becomes Eq. (24), after following similar steps to those discussed in section 2.1.1. Equation (24) is valid for every individual frequency sample, thus it is again put into a matrix form in Eq. (25) in order to force the nonlinear coefficients to be constant. The frequency sample number is, once again, indicated in the quantities' sub- or superscripts, e.g. $S_{QQ}(\Omega_s) = S_{QQ}^s$ or $D_k(\Omega_s) = D_k^s$.

$$D_k(\Omega)\ \mathbf{Q}_k\mathbf{Q}_k^H + \gamma_1^v\ \mathbf{P}_1^{v,k}\mathbf{Q}_k^H + \cdots + \gamma_1\ \mathbf{P}_1^k\mathbf{Q}_k^H + \cdots = \mathbf{\Psi}_k\mathbf{Q}_k^H \tag{23}$$

$$D_k(\Omega)\ S_{QQ} + \gamma_1^v S_{P_1^vQ} + \cdots + \gamma_1\ S_{P_1Q} + \cdots = S_{\Psi Q} \tag{24}$$

$$\underbrace{\begin{bmatrix} S_{QQ}^0 & & & S_{P_1^vQ}^0 & & S_{P_1Q}^0 & \\ & \ddots & & \vdots & \cdots & \vdots & \cdots \\ & & S_{QQ}^n & S_{P_1^vQ}^n & & S_{P_1Q}^n & \end{bmatrix}}_{\mathbf{S}_{D2}^{auto}} \begin{bmatrix} D_k^0 \\ \vdots \\ D_k^n \\ \gamma_1^v \\ \vdots \\ \gamma_1 \\ \vdots \end{bmatrix} = \underbrace{\begin{bmatrix} S_{\Psi Q}^0 \\ \vdots \\ S_{\Psi Q}^n \end{bmatrix}}_{\mathbf{S}_{D2}^{cross}} \tag{25}$$

Note that the system of equations (25) suffers form the same indeterminacy issues as those seen in Eq. (16). To overcome them, one can once again use r sets of measurements to create an over-determined system as in the previous section. Doing so, one obtains the linear systems in Eqs. (26) and (27), where

the nonlinear parameters occur as complex and real numbers, respectively. The quantities $\boldsymbol{\sigma}_{D2}^{auto}$ and $\boldsymbol{\sigma}_{D2}^{cross}$ from Eq. (27) are defined in Eqs. (28) and (29). Equations (26) and (27) are the base formulas for this version of the $\mathbf{D}_2$–NIXO method and can be solved via linear least squares.

$$\begin{bmatrix} \mathbf{S}_{D2,I}^{auto} \\ \\ \mathbf{S}_{D2,II}^{auto} \\ \\ \vdots \\ \\ \mathbf{S}_{D2,r}^{auto} \end{bmatrix} \begin{bmatrix} D_k^0 \\ \vdots \\ D_k^n \\ \gamma_1^v \\ \vdots \\ \gamma_1 \\ \vdots \end{bmatrix} = \begin{bmatrix} \mathbf{S}_{D2,I}^{cross} \\ \\ \mathbf{S}_{D2,II}^{cross} \\ \\ \vdots \\ \\ \mathbf{S}_{D2,r}^{cross} \end{bmatrix} \tag{26}$$

$$\begin{bmatrix} \boldsymbol{\sigma}_{D2,I}^{auto} \\ \\ \boldsymbol{\sigma}_{D2,II}^{auto} \\ \\ \vdots \\ \\ \boldsymbol{\sigma}_{D2,r}^{auto} \end{bmatrix} \begin{bmatrix} D_k^0 \\ \vdots \\ D_k^n \\ \gamma_1^v \\ \vdots \\ \gamma_1 \\ \vdots \end{bmatrix} = \begin{bmatrix} \boldsymbol{\sigma}_{D2,I}^{cross} \\ \\ \boldsymbol{\sigma}_{D2,II}^{cross} \\ \\ \vdots \\ \\ \boldsymbol{\sigma}_{D2,r}^{cross} \end{bmatrix} \tag{27}$$

$$\boldsymbol{\sigma}_{D2}^{auto} = \begin{bmatrix} Re\{S_{QQ}^0\} & -Im\{S_{QQ}^0\} & & & Re\{S_{P_1^vQ}^0\} & & Re\{S_{P_1Q}^0\} & \\ Im\{S_{QQ}^0\} & Re\{S_{QQ}^0\} & & & Im\{S_{P_1^vQ}^0\} & & Im\{S_{P_1Q}^0\} & \\ & & \ddots & & \vdots & \cdots & \vdots & \cdots \\ & & & Re\{S_{QQ}^n\} & Re\{S_{P_1^vQ}^n\} & & Re\{S_{P_1Q}^n\} & \\ & & & Im\{S_{QQ}^n\} & Im\{S_{P_1^vQ}^n\} & & Im\{S_{P_1Q}^n\} & \\ & & & & & & & \end{bmatrix} \tag{28}$$

$$\boldsymbol{\sigma}_{D2}^{cross} = \begin{bmatrix} Re\{S_{\Psi Q}^0\} \\ Im\{S_{\Psi Q}^0\} \\ \vdots \\ Re\{S_{\Psi Q}^n\} \\ Im\{S_{\Psi Q}^n\} \end{bmatrix} \tag{29}$$

2.2 Summary of the Algorithms

To understand the benefits of the proposed NIXO algorithms, this work compares them to the well-known and popular NIFO algorithms (which are derived in Appendix A) and to the linear $\mathbf{H}$ estimators. The two versions of each algorithm are used, denoted the $\mathbf{D}_1$ and $\mathbf{D}_2$ algorithms for NIXO and the $\mathbf{H}_1$ and $\mathbf{H}_2$ for NIFO and linear estimators. Note that the choice of whether to use an $\mathbf{D}_1/\mathbf{H}_1$ or $\mathbf{D}_2/\mathbf{H}_2$ approach is usually dictated by the noise present in the input or output signals [45]; in this work both are demonstrated in various cases. Additionally, the NIXO algorithms can be forced to identify the nonlinear parameters as real numbers, or they can estimate a complex number and then take the real part. Considering all of these varieties, there are 8 different possible algorithms that will be compared in the case studies that follow.

It is also worth noting that additional variations on the NIXO and NIFO algorithms' are possible. If the linear natural frequencies and damping ratios are known, then these can be used to reconstruct the linear dynamic stiffness or frequency response function and provide them to the NIXO/NIFO algorithms.

This variation was explored and called the Linear-Data-Provided, or LDP variation. Additionally, NIFO could also use multiple data sets as is done in NIXO or it could use just one. Finally, there are at least three different algorithms that could be used to solve the resulting set of linear equations. An in-depth comparison of the 40 different possible algorithms is elaborated in the extended version of this article [44]. To avoid overwhelming the reader with too much data, this work presents only those variations of the above mentioned algorithms that gave the best results, specifically: NIXO combined with the least squares solver and NIFO with the linear equations solved using QR decomposition. The case studies also demonstrated, as one might expect, that it was important that the structures vibrates at high enough amplitudes so that the nonlinearities are exercised [44].

2.3 Validating the Identified Nonlinear Models

Nonlinear normal modes (NNMs) are used in this work to compare the various nonlinear models that are identified from measurements, and also to qualitatively assess the accuracy of the models. Nonlinear normal modes were first defined by Rosenberg [46–49] and his definition was relaxed in by Vakakis et al. [50–52], defining an NNM as a not-necessarily synchronous periodic motion of a conservative system [53].

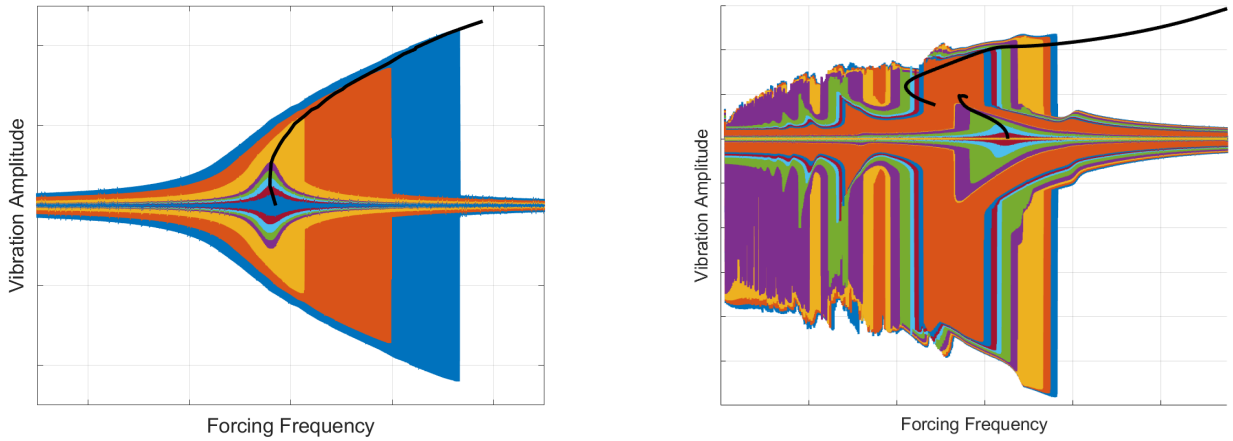

(a) **(b)**

Fig. 1: Swept sine signals of various amplitudes, each shown with a different color, applied to a structure exhibiting **(a)** stiffening and **(b)** softening-stiffening characteristics. The nonlinear normal mode is also overlaid (solid black line) and in most cases its location can be inferred from the swept sine measurements.

One of the simplest ways to estimate the NNM backbone curve of a system (or simply to check if the structure behaves nonlinearly) is to subject the structure to swept sines of different forcing amplitudes, as illustrated in Fig. 1. Such an approach is not very robust because of the *"premature jump phenomenon"* [54], and it may not work if the system exhibits softening-stiffening characteristics, but it is simple and often is quite effective. It is used here to give the reader a qualitative view of the strength of the nonlinearity in each experimental or simulated measurement.

3 Numerical Investigation: SDOF system

The algorithms were first evaluated using input and output signals collected during simulated experiments on an SDOF system. The equation of motion for the system of interest is given in Eq. (30), and the forcing is defined in Eq. (31). The values of the system parameters used are summarized in Tab. 1. Note that in

the extended version of this article [44], a simpler system where $c_2 = 0$ and $k_2 = 0$ was studied and the results were more or less similar.

$$m\ddot{x} + c\dot{x} + kx + c_2\dot{x}^2 + k_2x^2 + k_3x^3 = f(t) \tag{30}$$

$$f(t) = F\cos(\Omega(t)t) \qquad F \in \{F_1,\ F_2\} \qquad \Omega(t) = \Omega_0 + \frac{\Omega_f - \Omega_0}{t_f - t_0}(t - t_0) \qquad t \in [t_0,\ t_f] \tag{31}$$

Tab. 1: Parameters used for the numerical SDOF system and those defining the swept-sine input signals.

m [kg]	$c\left[\frac{\text{Ns}}{\text{m}}\right]$	$k\left[\frac{\text{N}}{\text{m}}\right]$	$c_2\left[\frac{\text{Ns}^2}{\text{m}^2}\right]$	$k_2\left[\frac{\text{N}}{\text{m}^2}\right]$	$k_3\left[\frac{\text{N}}{\text{m}^3}\right]$
1	0.2	1	0.5	0.3	0.5

F_1 [N]	F_2 [N]	Ω_0 [Hz]	Ω_f [Hz]	t_0 [s]	t_f [s]
1.0	0.1	$\frac{0.01}{2\pi}$	$\frac{3}{2\pi}$	0	500

In every test, the initial conditions were $x(0) = 0,\ \dot{x}(0) = 0$ and the system was excited by a swept sine signal at a certain amplitude. Then, the signals corresponding to two distinct amplitudes, $\{F_1,\ F_2\} = \{1.0,\ 0.1\}\ N$, were provided to the algorithms. The sweeps were each 500 seconds long and they covered the frequency range from 0.01 to 3 rad/s. This frequency range was chosen to encompass the linear natural frequency at 1 rad/s. The input and output signals are shown in Fig. 2. Note that the response of the system is clearly not symmetric due to the quadratic nonlinearity in Eq. (30).

These signals were then used to populate Eq. (12) by applying a 240-second-long Hann window with an overlap of 50% to each time signal. This resulted three spectral averages (per signal), $N_{avg} = 3$. Each of the averages consisted of 1201 frequency lines ranging from 0 to 10π rad/s ($n = 1201$).

The size of the linear system of equations that NIXO needs to solve is a multiple of $(n+1)$ (see Eqs. (16) and (18)), where $n = 1201$. In contrast, NIFO solves 1201 much smaller linear systems of equations (one for each individual frequency line), each of which is independent from all others, as shown for example in Eq. (B2). To reduce the size of these algebraic problems, after the spectral averages were obtained for the full range of frequency, the frequency range used in the identification can be narrowed, speeding up both algorithms. This also focuses the identification on the measurements near resonance, which typically contain the best signal to noise ratio. In this particular case, frequency range was narrowed from $(0,\ 10\pi)$ to $(0.01,\ 3)$ rad/s, reducing the problem size from 1201 to 114 frequency samples.

To provide the reader with a visual indication of the level of nonlinearity in the system, the linear $\mathbf{H}_1$-estimator was first applied to the measurements and the results are shown in Fig. 3a. The estimated linear frequency response functions (FRFs) match the true linear FRF well. To quantify this, the natural frequency and damping ratio were estimated from the linear FRFs using the Algorithm of Mode Isolation (AMI) [55] and the results are shown in Tab. 2. They agree well with the true modal natural frequency and damping ratio, having less than 1% and 6% error, respectively, in every case. On the other hand, when input/output signals of higher amplitude are provided to the **H**-estimators, they return an estimates of the linear FRFs that are distorted by the nonlinearities, as seen in the dashed lines in Fig. 3, and so no attempt was made to fit a linear model to that measurement. It is worth noting that some systems are essentially nonlinear [56, 57], so that a linear range does not exist; such a system might not exhibit linear behavior at any vibration amplitude.

Next, NIXO was applied to the pair of measurements (high and low amplitude), assuming a model that had three nonlinear terms, c_2, k_2, and k_3, as in Eq. (30). The underlying linear FRFs estimated by

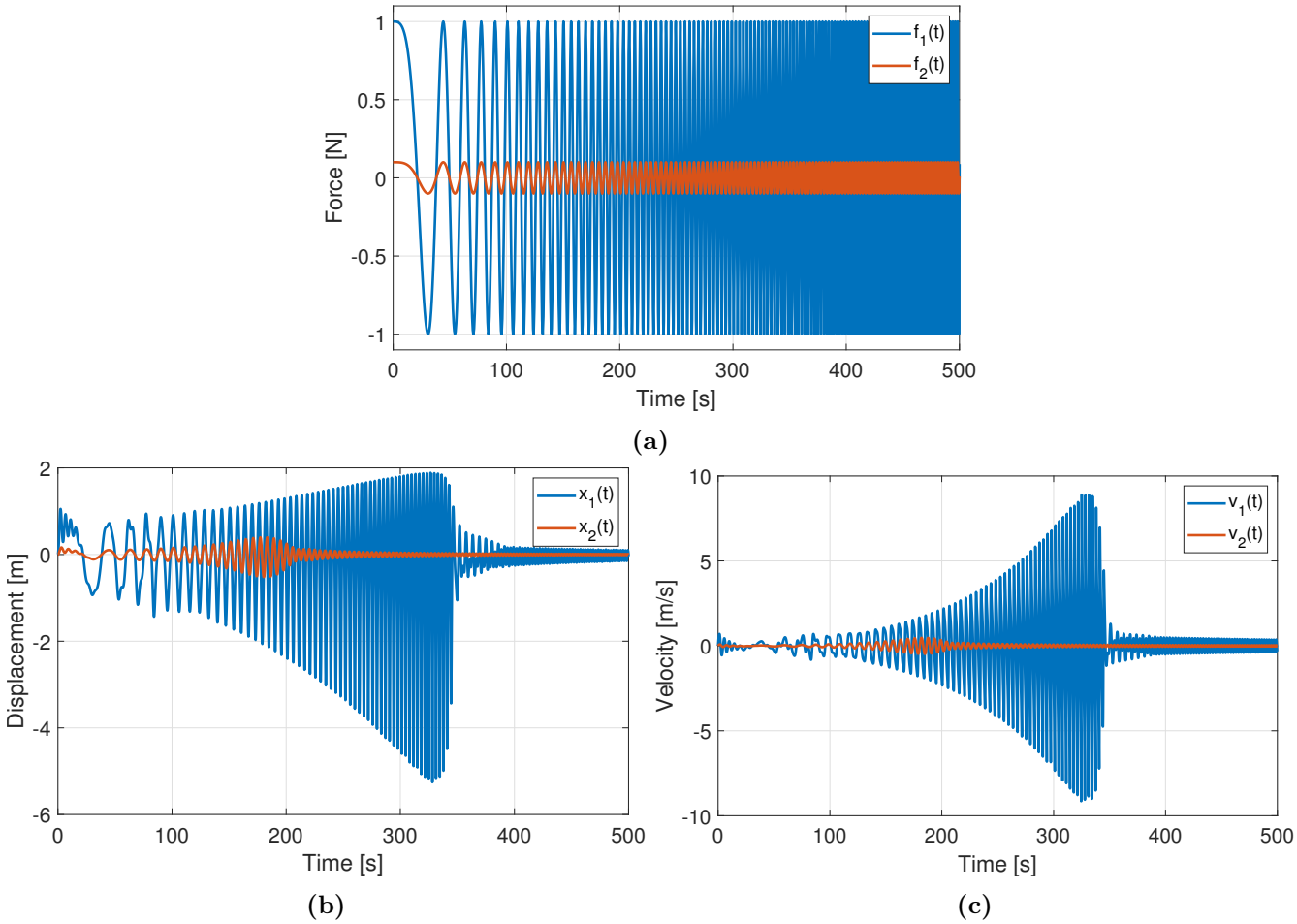

Fig. 2: Simulated input and output signals used in the SDOF system case study. Subplot **(a)** presents the forcing signals: $f_1(t)$ and $f_2(t)$. Subplots **(b-c)** show the output displacement and velocity signals generated by integrating Eq. (30). That output signals $x_1(t)$ and $v_1(t)$ are the response to forcing $f_1(t)$ and $x_2(t)$ and $v_2(t)$ are due to $f_2(t)$.

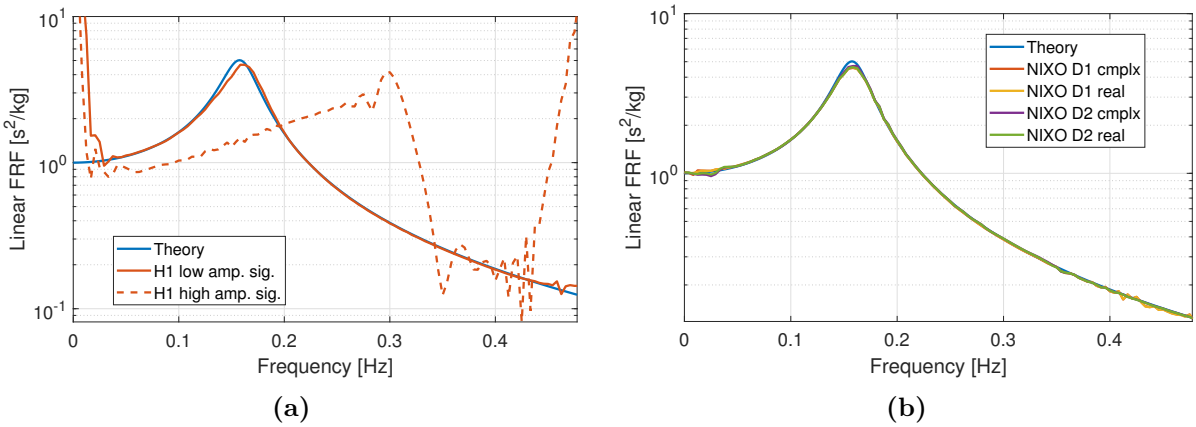

Fig. 3: The estimates of the underlying linear system obtained with the **(a)** linear $\mathbf{H}_1$-estimator and **(b)** NIXO algorithms. The results are compared to the true frequency response function.

the NIXO algorithms are presented in Fig. 3b, and once again the linear modal parameters were extracted from them using AMI and are shown in Tab. 2. The relative error between them does not exceed 3% for f_{lin} and 8% for ζ_{lin}, confirming the accuracy of the linear FRFs estimated by NIXO. When it comes to the nonlinear part of the system, NIXO identified all three nonlinear coefficients with relative error lower than 2%, as shown in Tab. 3. There was not a clear pattern regarding whether NIXO was more accurate when forcing the nonlinear parameters to be real rather than complex, so it appears that either approach may be viable.

Tab. 2: The quantitative comparison of the linear frequency response function presented in Fig. 3. The relative difference calculated with respect to the true values of the linear natural frequency and damping ratio.

	f_{lin} [Hz]	(rel. diff. [%])	ζ_{lin}	(rel. diff. [%])
Theory	0.1592		0.1	
H1	0.1584	0.47	0.1055	5.45
D1 cmplx	0.1547	2.79	0.1056	5.64
D1 real	0.1548	2.77	0.1049	4.86
D2 cmplx	0.1550	2.60	0.1018	1.79
D2 real	0.1548	2.71	0.1041	4.11

Tab. 3: The estimates of the nonlinear c_2, k_2, and k_3 parameters obtained with the NIXO algorithms.

NIXO	c_2 $\left[\frac{\text{Ns}}{\text{m}}\right]$	(rel. diff.)	k_2 $\left[\frac{\text{N}}{\text{m}^2}\right]$	(rel. diff.)	k_3 $\left[\frac{\text{N}}{\text{m}^3}\right]$	(rel. diff.)
D1 (real)	0.2996	0.12 %	0.3005	0.18	0.5016	0.33 %
D1 (cmplx)	$0.2977 + i\ 0.0034$	0.78 %	$0.2985 + i\ 0.0073$	0.49	$0.5001 + i\ 0.0019$	0.02 %
D2 (real)	0.3006	0.21 %	0.2959	1.37	0.4994	0.12 %
D2 (cmplx)	$0.3006 + i\ 0.0022$	0.21 %	$0.2981 + i\ 0.0114$	0.63	$0.4999 + i\ 0.0065$	0.01 %

For comparison purposes, the NIFO algorithm was also applied to these measurements and the results are shown in Fig. 4. The NIFO algorithms were applied to the high amplitude signals (i.e. those generated when $F_1 = 1\ N$). Figure 4 shows that the NIFO estimates of both the underlying linear FRF as well as the nonlinear part of the system are highly inaccurate. The results obtained with the NIFO-based methods are consistent with the authors' other experiences trying to use this technique in case studies with the swept-sine input signals. (In the extended version of this manuscript [44], NIFO was applied to a nonlinear SDOF system that contained only a cubic nonlinearity and the results were better than those shown here but still far from ideal.) It is worth noting that although the NIFO algorithms did not work well in this case study, in which the system was excited with a swept-sine input, other case studies were also run in which they did work well. Specifically, when a random broadband input was applied to this and similar systems the NIFO algorithms gave results that were quite comparable to those shown above for NIXO. This was documented in [58] as well as in the publications of other authors [39,59]. Moreover, a case study where NIFO accurately identifies a structure excited with a random input is presented in section 4 of this work.

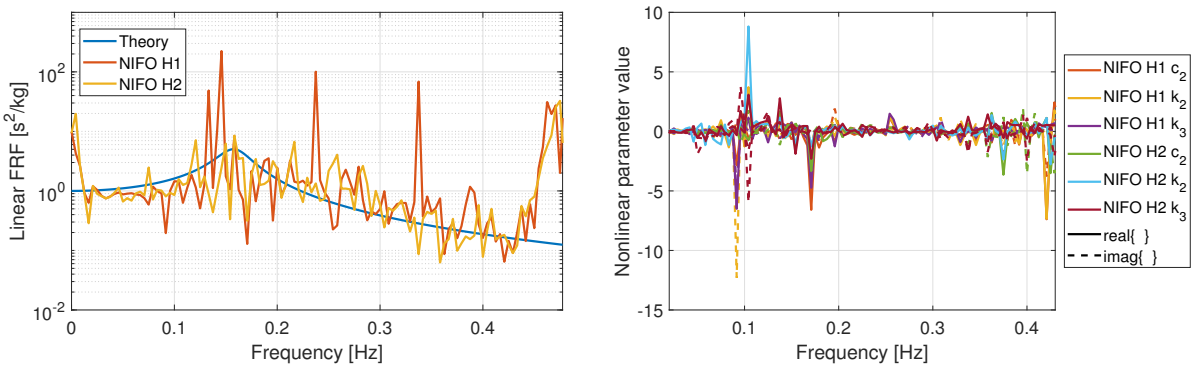

(a) **(b)**

Fig. 4: The estimates of the underlying linear system and nonlinear c_2, k_2 and k_3 parameters obtained with the NIFO algorithms.

4 Numerical Investigation: Flat Clamped-Clamped Beam with Cubic Nonlinearity

In order to evaluate the performance of the algorithms for a multi-degree-of-freedom system, they were also tested using simulated measurements from a two-mode ICE-ROM of a flat beam with clamped-clamped boundary conditions, see Fig. 5. The beam is similar to the one studied in [37, 39, 59], and its dimensions were $228.6 \times 12.7 \times 0.787$ mm (length $\times$ width $\times$ thickness) with Young's modulus, density and shear modulus being 2.05×10^{11} Pa, 7866 kg/m^3 and 8.0×10^{10} Pa, respectively.

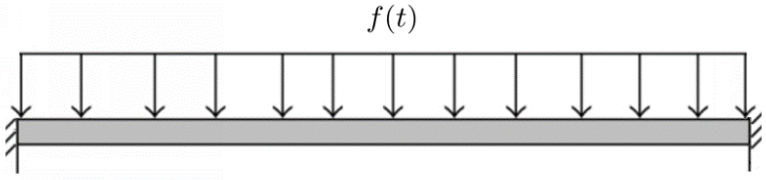

Fig. 5: Numerical model of a clamped-clamped flat beam excited with a uniformly distributed force.

The structure was modeled with 40 beam elements (resulting in a total of 246 DOFs) and the finite element model was used to generate a 2-mode ICE-ROM including the first two symmetric modes, i.e. modes 1 and 3. It was subjected to a forcing that was uniformly distributed in space, as depicted in Fig. 5, and which models a base excitation, and was either sinusoidal or random in time. Equation (32) presents the nonlinear equations of motion expressed in the modal domain, which nonlinear part consists of four cubic terms. Table 4 displays their values together with those describing the underlying linear system. The units of the nonlinear β-coefficients used in this work are always kg^{-1}m^{-2}s^{-2}. Their units are provided in Tab. 4 but, for brevity, will be omitted in all other Tables and Figures.

$$\begin{cases} \ddot{q}_1 + 2\zeta_1\omega_1\dot{q}_1 + \omega_1^2 q_1 + \beta^1_{111}q_1^3 + \beta^1_{112}q_1^2 q_2 + \beta^1_{122}q_1 q_2^2 + \beta^1_{222}q_2^3 = \mathbf{\Phi}_1^T\mathbf{f}(t) \\ \ddot{q}_2 + 2\zeta_2\omega_2\dot{q}_2 + \omega_2^2 q_2 + \beta^2_{111}q_1^3 + \beta^2_{112}q_1^2 q_2 + \beta^2_{122}q_1 q_2^2 + \beta^2_{222}q_2^3 = \mathbf{\Phi}_2^T\mathbf{f}(t) \end{cases} \tag{32}$$

Initial trials revealed that the algorithms performed differently for different types of inputs, so both swept-sine and broadband inputs were considered. Subsection 4.1 focuses on the case with swept-sine excitation, while subsection 4.2 on the case with the random forcing. As with the prior case studies, our

Tab. 4: Linear and nonlinear modal properties of the numerical flat beam. Nonlinear coefficients values expressed in $\mathrm{kg}^{-1}\mathrm{m}^{-2}\mathrm{s}^{-2}$.

	j	ω_j [Hz]	ζ_j	β_{111}	β_{112}	β_{122}	β_{222}
Mode 1	1	79.026	0.3 %	5.70×10^8	1.49×10^9	6.47×10^9	4.89×10^9
Mode 3	2	427.460	0.5 %	3.90×10^8	5.08×10^9	1.16×10^{10}	4.31×10^{10}

initial trials, documented in [44], revealed that nonlinear identification was only successful if the input signals had large enough amplitude, and so only those case studies are presented here.

4.1 Identification of Mode 1 Using Swept-Sine Forcing Functions

This section presents the outcomes from the case study where the beam is excited near its first NNM with a uniformly distributed *swept-sine* forcing function, defined in Eq. (33). The sweep rate, common to each input signal used, was equal 0.667 $\frac{\mathrm{Hz}}{s}$, see Eq. (34). The remaining parameters describing the case study are summarized in Tab. 5.

$$f(t) = F_k \cos(\Omega(t)t) \qquad \Omega(t) = \Omega_{st} + \frac{\Omega_{end} - \Omega_{st}}{t_{end}} t \qquad t \in [0,\ t_{end}] \tag{33}$$

$$\frac{\Omega_{end} - \Omega_{st}}{t_{end}} = const = \ 0.667\ \frac{\mathrm{Hz}}{\mathrm{s}}, \tag{34}$$

where t_{end} stands for the signal's length and can be calculated using Eq. (34) and information from Tab. 5.

Tab. 5: Parameters describing the high-amplitude swept-sine input signals used to excite the numerical flat beam system.

Test Type	F_1 [N]	F_2 [N]	Ω_{st} [Hz]	Ω_{end} [Hz]	Δt [s]
High-Amplitude	4.40×10^{-1}	2.20×10^{-1}	50	250	1.50×10^{-4}

Figure 6 shows the responses measured at the beam's center during the high-amplitude vibration tests. The beam experiences extreme deflections, since the maximum displacement of its center is larger than 5 times the beam's thicknesses. The well known jump phenomenon [54] occurs at approx. 241 Hz and 211 Hz when the beam is excited with signals of $F_1 = 4.40 \times 10^{-1}$ and $F_2 = 2.20 \times 10^{-1}$ N, respectively. This corresponds to the extreme nonlinear natural frequency absolute shifts of 305% and 267%, respectively.

In order to form the matrices required by NIXO, e.g. Eq. (12b), 15.75-second-long Hanning windows with an overlap of 50% were applied to each time series. This resulted in 94 spectral averages, each consisting of 52501 frequency samples. As in the previous section, in order to reduce the size of the linear system of equations solved by NIXO, only the data for frequencies in the range (50, 250) Hz was used. Based on the sample rate, the maximum frequency range was $(0,\ 3333\frac{1}{3})$ Hz with a total of 52501 frequency samples, so this reduced the number of equations to 3151, or by a factor of 16.7.

4.1.1 Results

Figure 7a shows the linear FRFs estimated using the linear $\mathbf{H}_1$-estimator as well as those estimated by NIXO. In this case, both the low and high amplitude signals excited the nonlinearity significantly, as seen in the linear $\mathbf{H}_1$ estimates, hence the linear natural frequency and damping ratio weren't estimated.

The linear FRF estimates obtained with NIXO are displayed in Fig. 7b and the natural frequencies and damping ratios estimated from them are shown in Tab. 6. The relative differences do not exceed 0.1%

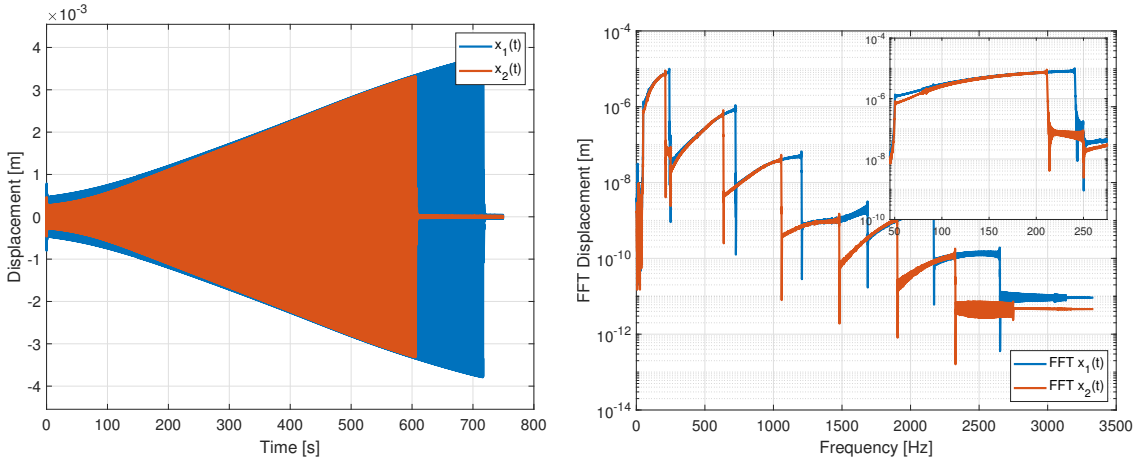

Fig. 6: Time and frequency representations of the output signals measured at the beam's center in the high-amplitude vibrations tests when the structure was excited with a swept-sine force.

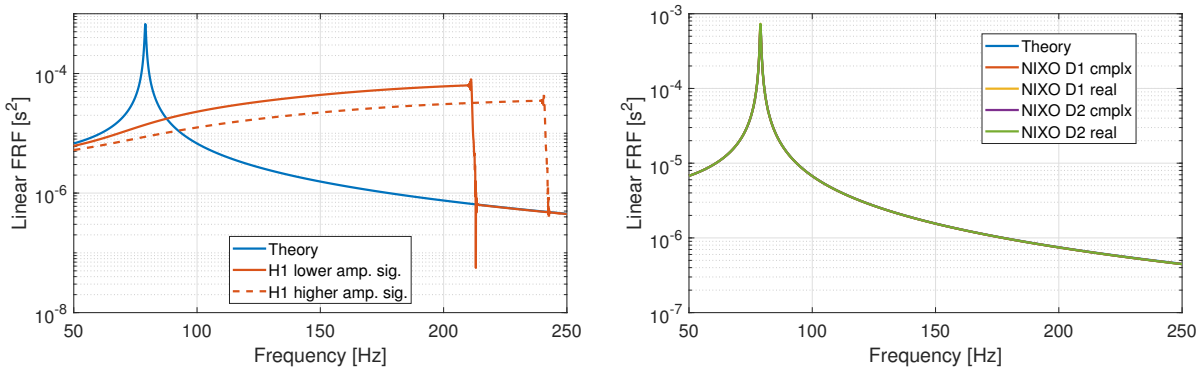

(a) **(b)**

Fig. 7: The estimates of the underlying linear system obtained with the **(a)** linear $\mathbf{H}_1$-estimator and **(b)** NIXO algorithms applied to the pair of swept-sine signals. The results are compared to the true frequency response function.

for the linear frequencies and 8% for the damping ratios, confirming that NIXO has accurately estimated the linear FRF from the measurements even though they show strong nonlinearity. Table 7 summarizes the nonlinear β-coefficients estimated by all four versions of NIXO. The largest error was less than 3% and most errors were far smaller.

Figure 8 presents the results returned by the NIFO methods. The content of the figure is organized as follows: the pane on the far left shows the linear FRFs estimated by the $\mathbf{H}_1$- and $\mathbf{H}_2$-variations of NIFO compared to the true FRF. The estimates of the nonlinear β-parameters (expressed as functions of frequency) are displayed in a two by two grid on the right hand side. Each column there shows the coefficients' real and imaginary parts, while the two rows present the parameters using the logarithmic and linear scales. A logarithmic scale is helpful in seeing whether there are frequency ranges where the parameters are or are not constant, while the parameters of interest are easiest to read on the linear scale.

The outcomes displayed in Fig. 8 show, once again, that the NIFO-based algorithms did not work well when the structure was excited with swept-sine signals (even if it oscillates at sufficiently high-levels to excite the nonlinearity). It seems that it is not advisable to use the NIFO identification approach when swept sine excitation is used.

Tab. 6: Linear natural frequencies and damping ratios estimated from the linear FRF curves in Fig. 7 and the errors relative to the true values. Identification was not applied to the results of the linear $\mathbf{H}_1$-estimator, so those results are marked with ($\times$).

	f_{lin} [Hz]	(rel. diff. [%])	ζ_{lin}	(rel. diff. [%])
True	79.0260		0.0030	
H1	$\times$	$\times$	$\times$	$\times$
D1 cmplx	78.9817	0.056%	0.0028	6.33%
D1 real	78.9793	0.059%	0.0028	7.39%
D2 cmplx	78.9787	0.060%	0.0030	1.55%
D2 real	78.9770	0.062%	0.0028	7.40%

Tab. 7: The estimates of the nonlinear β-parameters obtained with the $\mathbf{D}_1$- and $\mathbf{D}_2$-based NIXO algorithms applied to the swept-sine signals.

NIXO D1	β_{real}	(rel. error)	β_{cmplx}	(rel. error)
β_{111}	5.70e+08	(0.01%)	5.70e+08 - i 8.10e+04	(0.00%)
β_{112}	1.50e+09	(0.13%)	1.49e+09 - i 3.21e+05	(0.12%)
β_{122}	6.48e+09	(0.04%)	6.44e+09 + i 4.46e+07	(0.48%)
β_{222}	4.89e+09	(0.09%)	4.76e+09 + i 3.63e+08	(2.77%)

NIXO D2	β_{real}	(rel. error)	β_{cmplx}	(rel. error)
β_{111}	5.70e+08	(0.03%)	5.70e+08 - i 8.47e+05	(0.01%)
β_{112}	1.50e+09	(0.38%)	1.49e+09 - i 2.51e+07	(0.09%)
β_{122}	6.49e+09	(0.19%)	6.45e+09 - i 3.78e+07	(0.42%)
β_{222}	4.96e+09	(1.25%)	4.78e+09 - i 1.24e+08	(2.32%)

4.2 Identification of Mode 3 Using Random Forcing Functions

The beam was then excited with a uniformly distributed *random* forcing function, defined in Eq. (35), where $U_n(t)$ is uniform random variable in the range $[-1, 1]$. Each input signal was 120 seconds long and had a sample rate of $\Delta t = 9.00 \times 10^{-5}$ s.

$$f(t) = F^{rand} \times U_n(t) \qquad F^{rand} \in \{F_1^{rand},\ F_2^{rand}\} \qquad t \in [0,\ 120]\ \text{s} \tag{35}$$

Figure 9 shows the two responses, $x_1(t)$ and $x_2(t)$, measured at the beam's center, obtained using the inputs $\{F_1^{rand},\ F_2^{rand}\} = \{4.40 \times 10^{-1}, 2.20 \times 10^{-3}\}$ N, respectively. In the latter test, the maximum displacement of the beam's center is slightly larger than 1% of its thickness, thus the beam most likely stays in the linear regime. On the other hand, the maximum deflection due to the former input reaches 146% of beam's thickness, so that significant nonlinearity should be excited. Furthermore, when that signal is applied to the beam, the peak in the frequency spectra shifts to the right, as illustrated in Fig. 9.

To obtain the NIXO matrices in Eq. (12b), 6.3-second-long Hanning windows with an overlap of 50% were applied to each time series. This resulted in 37 spectral averages each consisting of 35001 frequency lines ranging from 0 to 5555.6 Hz. Then, the frequency range was narrowed to (390, 530) Hz reducing the size of the algebraic problem to be solved by NIXO by a factor of 39.6.

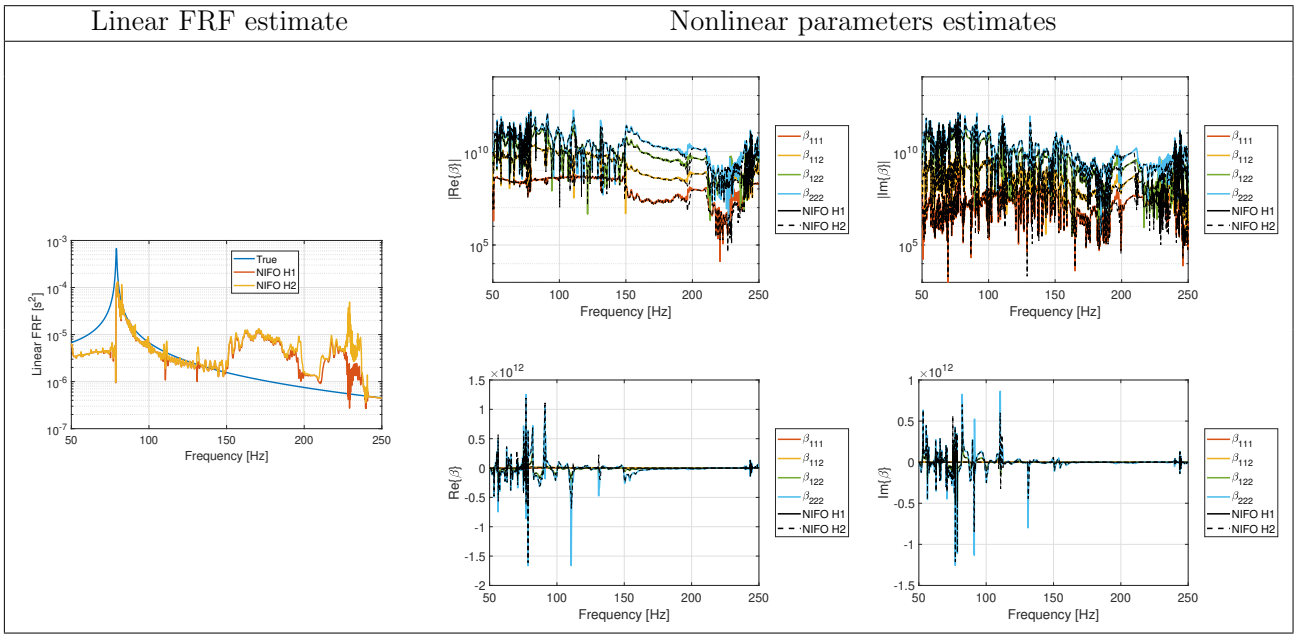

Fig. 8: The estimates of the underlying linear system and nonlinear β-parameters obtained with the NIFO algorithms using *high*-amplitude swept-sine input signals.

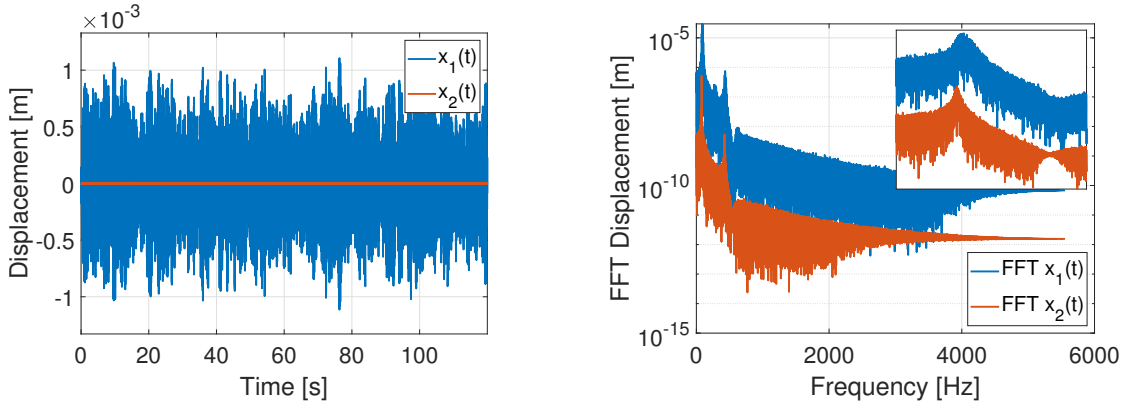

Fig. 9: Time and frequency representations of the output signals measured at the beam's center in the high-amplitude vibrations tests when the structure was excited with a random force.

4.2.1 Results

Figure 10a and Table 8 show the linear frequency response functions and natural frequencies and damping ratios as in prior sections. The linear $\mathbf{H}_1$ estimator nearly produces the underlying linear FRF when applied to the lower-level signals (corresponding to $F_2^{rand} = 2.20 \times 10^{-3} N$), and the relative errors between the natural frequency and damping ratio estimated from that FRF do not exceed 1%. In contrast, significant distortions are visible for $F_1^{rand} = 4.40 \times 10^{-1} N$, and so once again the linear modal parameters were not estimated from that measurement. Interestingly, the underlying linear FRFs estimated when NIXO was applied to the pair of input signals look very similar to that obtained by the $\mathbf{H}_1$ estimator for $F_2^{rand} = 2.20 \times 10^{-3} N$. All four NIXO algorithms produce results that are visually indistinguishable and are covered by the NIXO D2 real result shown in Fig. 10b. These results are all shifted to slightly lower frequencies

than the true FRF, but the relative errors in the linear natural frequencies and damping ratios estimated from them are all smaller than 1%, as seen in Table 8.

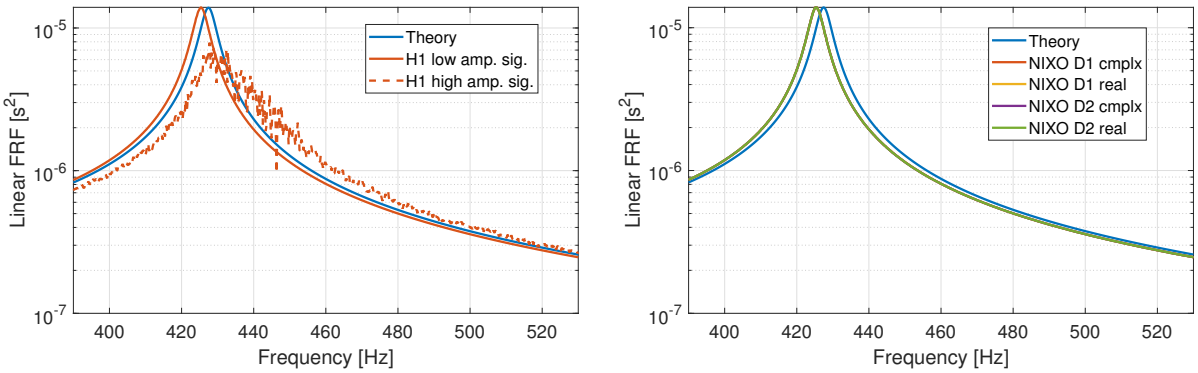

Fig. 10: The estimates of the underlying linear system obtained with the **(a)** linear $\mathbf{H}_1$-estimator and **(b)** NIXO algorithms applied to the burst random signals. The results are compared to the true frequency response function.

Tab. 8: The quantitative comparison of the linear FRFs presented in Fig. 10. The relative difference calculated with respect to the true values of the linear natural frequency and damping ratio.

	f_{lin} [Hz]	(rel. diff. [%])	ζ_{lin}	(rel. diff. [%])
True	427.4600		0.0050	
H1	424.8890	0.6015%	0.00496	0.831%
D1 cmplx	425.3758	0.4876%	0.00495	0.959%
D1 real	425.3756	0.4876%	0.00495	0.985%
D2 cmplx	425.3732	0.4882%	0.00495	0.955%
D2 real	425.3736	0.4881%	0.00496	0.861%

Table 9 lists nonlinear parameters identified by NIXO. The $\mathbf{D}_1$-based NIXO method found accurate (less than 3% error) values for all four β-parameters, while its $\mathbf{D}_2$-based twin estimated three of the

Tab. 9: The estimates of the nonlinear β-parameters obtained with the $\mathbf{D}_1$- and $\mathbf{D}_2$-based NIXO algorithms applied to the *high*-amplitude burst random signals.

NIXO D1	β_{real}	(rel. error)	β_{cmplx}	(rel. error)
β_{111}	3.89e+08	(0.34%)	3.89e+08 + i 1.08e+06	(0.36%)
β_{112}	5.07e+09	(0.14%)	5.07e+09 - i 4.66e+03	(0.13%)
β_{122}	1.13e+10	(2.63%)	1.12e+10 + i 3.34e+07	(2.68%)
β_{222}	4.35e+10	(0.98%)	4.33e+10 - i 5.29e+06	(0.65%)

NIXO D2	β_{real}	(rel. error)	β_{cmplx}	(rel. error)
β_{111}	3.73e+08	(4.38%)	3.75e+08 + i 5.28e+06	(4.01%)
β_{112}	5.04e+09	(0.74%)	5.04e+09 - i 1.80e+07	(0.76%)
β_{122}	9.14e+09	(20.91%)	8.99e+09 + i 8.91e+07	(22.19%)
β_{222}	4.45e+10	(3.28%)	4.46e+10 + i 2.75e+09	(3.47%)

four accurately. The methods that forced the parameters to be real gave similar results to those that identified complex parameters. It is worth noting that the case studies shown in [44] found that the $\mathbf{D}_2$-NIXO algorithm would identify a more accurate value for β_{122} if the forcing amplitude was increased. In contrast, if excitation signals of lower amplitudes were used, the algorithms would return the correct values of only one or two of the nonlinear coefficients.

Figure 11 presents the results obtained with the NIFO method. In contrast to the prior case study where swept-sine signals were used, for the random input signals the NIFO algorithm estimated the underlying linear FRF very accurately. Furthermore, the real parts of all four β-parameters were estimated as *nearly constant* functions of frequency and the imaginary parts of these β-frequency functions are a few orders of magnitude smaller then their real-counterparts. Hence, one could take the mean of these frequency-varying functions to estimate the desired nonlinear parameters. The mean values of these β-frequency functions are summarized in Tab. 10 (the averages were taken over the [390, 530] Hz frequency range). The relative error between their true and estimated values was less than 1% for all four nonlinear parameters. Similar to what occured for NIXO, if the amplitude of the random forcing was decreased, then NIFO would accurately estimate only some of the four β-parameters; the others would show significant variation with frequency and inaccurate average values [44].

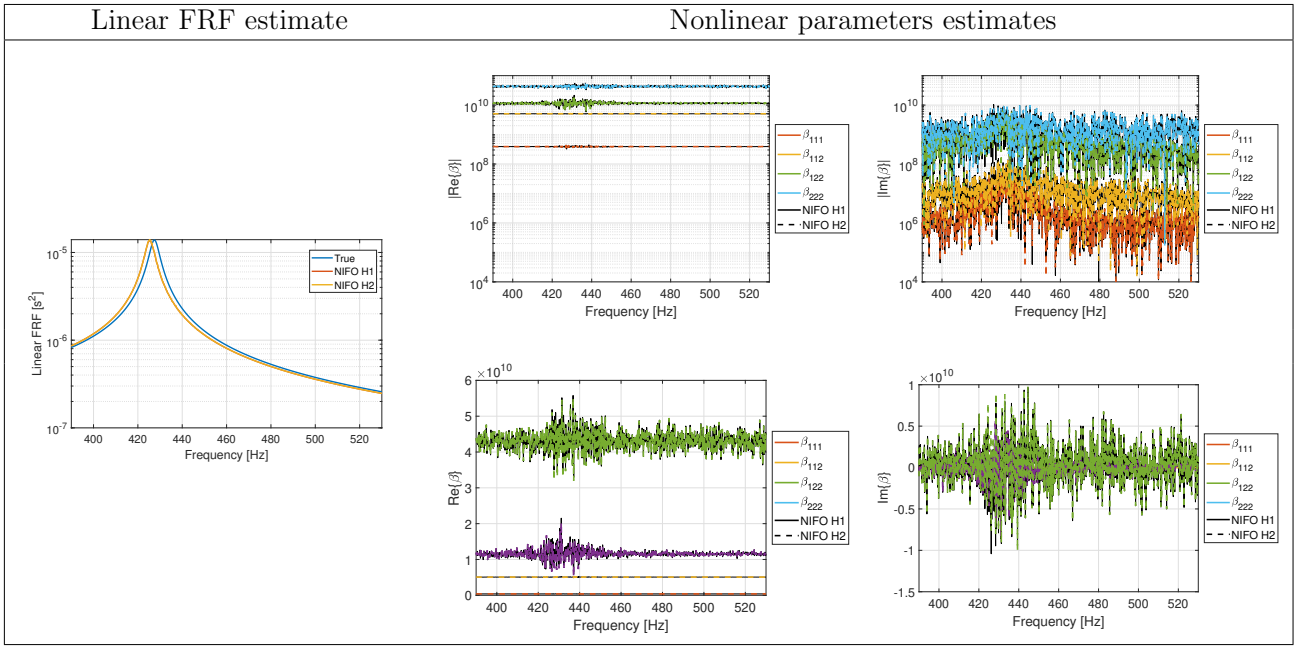

Fig. 11: The estimates of the underlying linear system and nonlinear β-parameters obtained when the NIFO algorithms were applied to the signals with random excitation of $F_1^{rand} = 4.40 \times 10^{-1}$ N.

Tab. 10: Nonlinear parameters obtained by NIFO by averaging the values in Fig. 11 over the (390, 530) Hz frequency range.

$Re\{\cdot\vert_{avg}\}$	NIFO-H1	(rel. error)	NIFO-H2	(rel. error)
β_{111}	3.90e+08	(0.03%)	3.90e+08	(0.05%)
β_{112}	5.08e+09	(0.03%)	5.08e+09	(0.00%)
β_{122}	1.16e+10	(0.67%)	1.16e+10	(0.05%)
β_{222}	4.31e+10	(0.13%)	4.30e+10	(0.07%)

4.3 Performance Analysis

Table 11 presents a comparison of the computational time NIXO and NIFO needed to solve the three numerical case studies. All calculations were run on a standard desktop computer using Intel® Core™ i7-8550U CPU processor. In all cases the computation time of the NIXO algorithm is similar to that of NIFO. This is surprising, as the NIXO algorithm solves one much larger linear system while NIFO inverts a much smaller system, although NIFO must repeat that inversion at every frequency line. Because the time needed to solve a linear system typically scales with the square of the size of the matrix, one would expect NIXO to be slower. However, this outcome could be explained by the fact that Matlab solves linear systems of equations by sending them to libraries of highly optimized routines while all of the data transfer required to set up thousands of smaller linear systems happens in the slower scripting environment.

Tab. 11: Computation times for NIXO and NIFO for various case studies.

Case	i	NIXO-D$_i$ [s]	NIFO-H$_i$ [s]	Ratio NIXO/NIFO
SDOF system with swept sine input	1	15.1	14.3	1.05
	2	20.1	17.0	1.18
Numerical beam with swept sine input	1	15.1	14.3	1.05
	2	20.1	17.0	1.18
Numerical beam with burst random input	1	2781	4904	0.57
	2	3433	5057	0.68

5 Experimental Investigation: Identification of 3D-Printed Flat Beam

The experimental set-up considered here is shown in Fig. 12a. The structure was excited using a Modal Exciter 100 lbf Model 2100E11 powered by a 2050E05 Linear Power Amplifier. The voltage input signal was generated using Polytec software and then sent to the shaker. The motion was measured at the three points of the beam; namely, the PSV-400 Scanning Vibrometer recorded the velocity at the beam's center, while two PCB352C23 accelerometers (attached to the structure) recorded the vibrations of the points located 37.08 millimeters from the beam's ends (see also Fig. 12b).

Figure 12 also shows the 3D-printed polylactide (PLA) sample used in the experiment. The thin and thick parts of the sample, called respectively beam and backing, are 3D-printed together as one piece. This prevents the beam's ends from slipping even when it oscillates at high amplitudes, so that the nonlinearity is purely geometric. When bolted joints are used as in [37] then one has to take care that the joints do not slip. That said, bolted structures are an important source of nonlinearity in industry and would certainly be of interest in a future work, but this study focuses on geometric nonlinearity only.

Tab. 12: Nominal dimensions and masses of the 3D printed sample and accelerometers.

	Length [mm]	Width [mm]	Thickness [mm]	Approx. mass [g]	Approx. mass of one accelerometer [g]
Beam	180	8	2	3.7696	0.1984
Backing	200	30	30	130.00	

The estimated mass and nominal dimensions of the 3D-printed sample and accelerometers are summarized in Table 12. It is worth noting that the beam's dimensions are nominal and subject to variation due to the

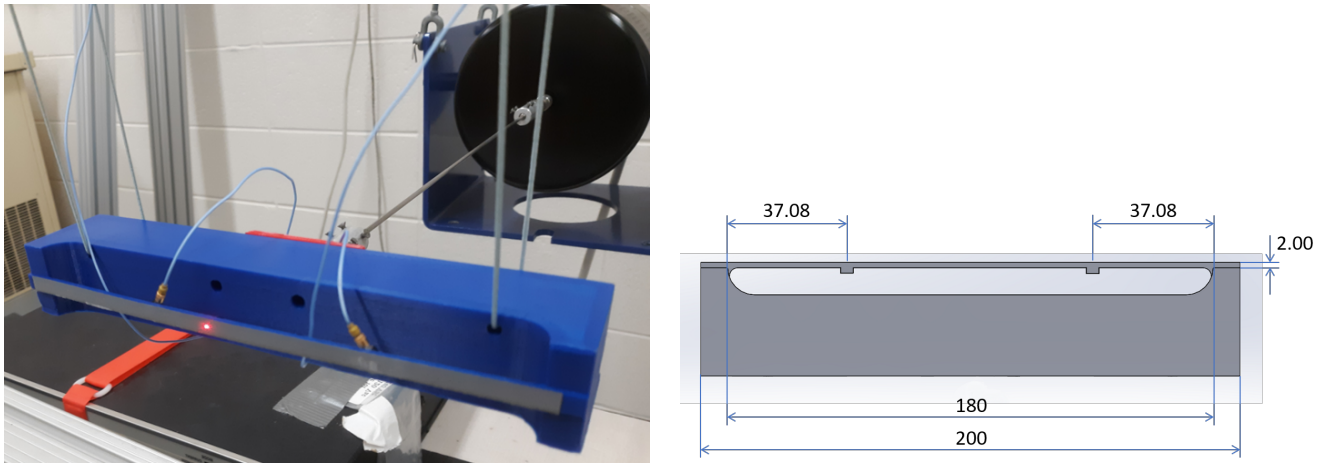

(a) **(b)**

Fig. 12: Photographs of **(a)** the experimental setup and **(b)** the longitudinal cross-section of beam model with the accelerometers attached.

3D printing process. The mechanical properties, such as the Young's modulus and Poisson ratio, would also be difficult to know precisely as they depend on the manufacturing process. Instead of measuring these quantities, the dynamic properties of the system, consisting of the sample with the attached accelerometers, are defined using their linear modal parameters, which were extracted from the frequency response function in Fig. 13 and are summarized in Table 13.

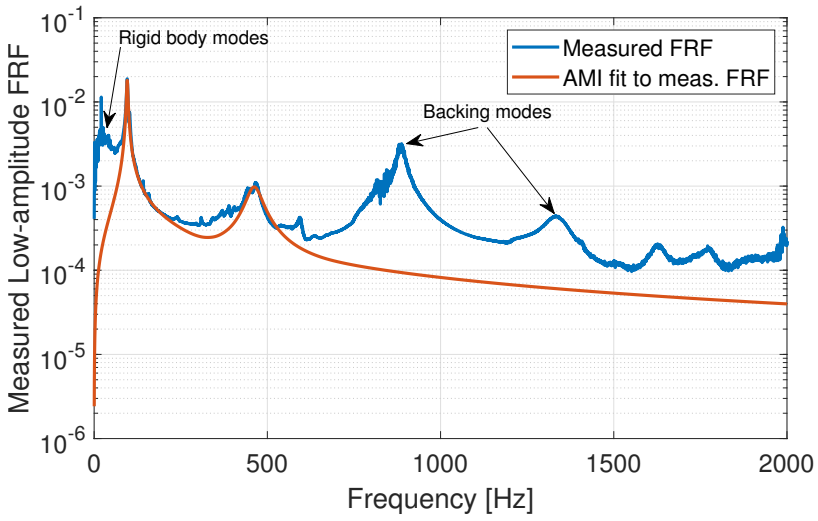

Fig. 13: Measured low-amplitude FRF of the beam-accelerometer assembly. Fit to the FRF computed using the Algorithm of Mode Isolation (AMI) [55]. The fit is done to the first two peaks only, since those are the modes of primary interest. The peaks at 887.5 and 1337.0 Hz are the modes of the backing.

A steel stinger connected the sample to the shaker. Moreover, the samples were designed such that the backing part can be modeled as a rigid body in the frequency range of the modes of interest. This allows the external point-force, which was applied via the stinger to the center of the backing, to be converted into a uniformly distributed force acting on the beam, see Fig. 14. The geometry of the beam-accelerometer assembly is represented with 3 points that correspond to the locations of the two accelerometers and laser.

Tab. 13: Linear modal properties of the flat beam-accelerometer assembly.

Mode ID	$\omega_{0,k}$ [Hz]	ζ_k	Mode shape
1	91.076	0.0119	1st bending of thin clamped-clamped beam
2	462.6952	0.0466	3rd bending of thin clamped-clamped beam (2nd symmetric bending)

In the tests performed, the Polytec software system was used to excite the structure with swept-sines of different amplitudes and to record the time responses.

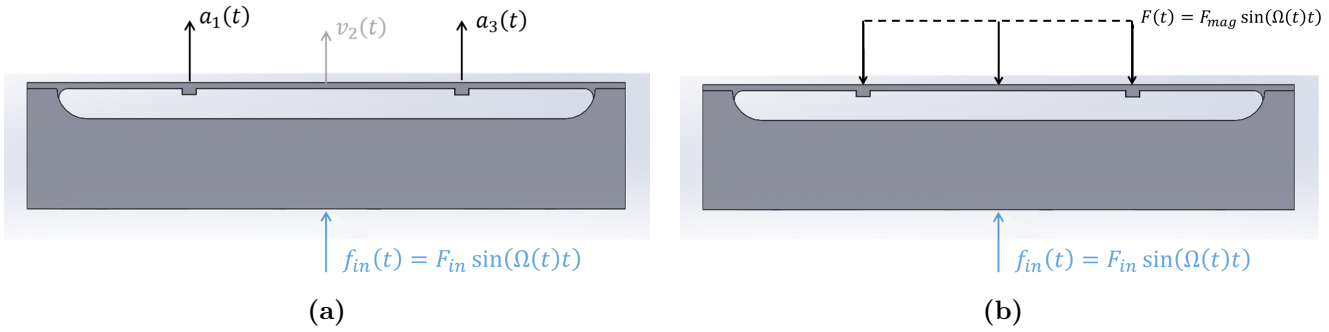

Fig. 14: **(a)** Locations of the input and output channels and **(b)** visualization of the external point-force applied at the backing's center being converted into a distributed inertial force.

5.1 Conversion of the Input Voltage Signal into a Distributed Force

In order to model the system with a reduced order model as was done in Sec. 4, the point force applied to the beam backing was converted into a distributed forcing acting on the thin beam. The conversion was validated using low amplitude measurements as described below. As presented in Fig. 15, measurements were performed with four low level swept-sine input signals and the results were used to validate the conversion.

The low-level responses were measured on the beam for input voltages $F_{in} \in \{0.010,\ 0.015,\ 0.025,\ 0.050\}$ volts, and are shown in Fig. 15. Then, a distributed force $\mathbf{F} = F_{mag}[1,1,1]^{\mathrm{T}}$ was applied to a linear modal model, Eq. (36), for the structure and F_{mag} was adjusted until the two agreed. The resulting values of F_{mag} were $\{1.6670,\ 2.8763,\ 5.1968,\ 11.054\} \times 10^{-3}$ newtons. The F_{mag} data was then expressed as a function of F_{in} as shown in Fig. 15b together with the linear regression fit showing that $F_{mag} \approx 0.2343 F_{in} - 6.5897 \times 10^{-4}$ – where F_{mag} and F_{in} are expressed in newtons and volts, respectively. It is worth noting that Fig. 15a shows that the tested sample exhibits slight frequency shifts even when the oscillations are low-level. Nevertheless, the linear system model, Eq. (36), with the parameters $\omega_{0,1}$ and ζ_1 adjusted accordingly, was assumed to be adequate to estimate the voltage-force conversion.

$$\mathbf{V}_{lin}^{theory} = \sum_{k=1}^{N_{RB}} \frac{-\boldsymbol{\Phi}_k^{RB}\left(\boldsymbol{\Phi}_k^{RB}\right)^T \mathbf{F}}{\Omega} \quad + \quad \sum_{k=1}^{N_{lin}} \frac{\boldsymbol{\Phi}_k \boldsymbol{\Phi}_k^T \mathbf{F}\Omega}{\omega_{0,k}^2 - \Omega^2 + 2i\zeta_k\omega_{0,k}\Omega}, \tag{36}$$

where $\boldsymbol{\Phi}_k$ and $\boldsymbol{\Phi}_k^{RB}$ are, respectively, the k-th columns of the mass-normalized elastic and rigid body mode shapes presented in Eq. (37).

$$\mathbf{\Phi} = [\mathbf{\Phi}_1, \mathbf{\Phi}_2] = \begin{bmatrix} 10.60 & 22.58 \\ 25.96 & -20.99 \\ 10.60 & 22.58 \end{bmatrix} \frac{1}{\sqrt{\text{kg}}} \tag{37a}$$

$$\mathbf{\Phi}^{RB} = \mathbf{\Phi}_1^{RB} = \begin{bmatrix} 8.633 \times 10^{-2} \\ 8.633 \times 10^{-2} \\ 8.633 \times 10^{-2} \end{bmatrix} \frac{1}{\sqrt{\text{kg}}} \tag{37b}$$

The relation between these two quantities does not have to stay linear with increasing vibration amplitude [60]. However, in the author's previous work on a different nonlinear system identification method [22] the experimental tests were run using the same shaker and very similar beams. Moreover, the voltage was converted into evenly distributed force using similar idea to that presented in this section, and the nonlinear normal modes of the object were successfully identified up to the input signals exceeding 300 mV. Hence, the linear conversion between the voltage and forcing is assumed to be accurate enough for the case study presented in this work.

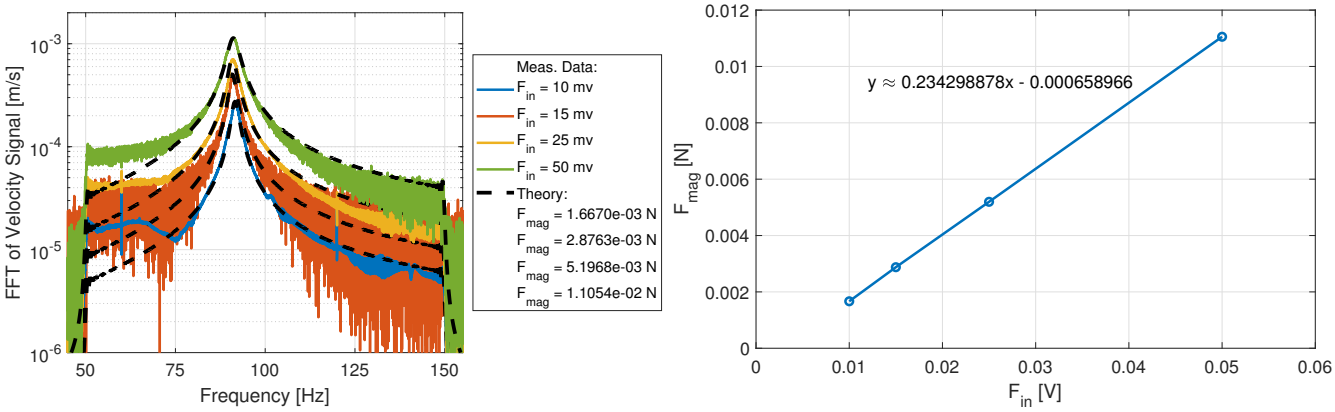

(a) **(b)**

Fig. 15: Comparison of **(a)** the low level velocity response measured at the beam's center and modeled using Eq. (36). Chart **(b)** presents the input voltage amplitudes that were applied to the backing and the corresponding force magnitudes used in the model, as well as a linear regression.

5.2 Identification of Mode 1 Using Swept-Sine Forcing Functions

5.2.1 Distinguishing Between the Coherent and Incoherent System ID Attempts

To identify the first nonlinear mode of the beam-accelerometer assembly, the modal equation of motion presented in Eq. (38) is postulated. It contains the usual linear terms and a single cubic nonlinear term. Because the beam is flat, it is reasonable to assume that the nonlinearity is only cubic.

$$\ddot{q}_1 + 2\zeta_1\omega_1\dot{q}_1 + \omega_1^2 q_1 + \beta_{111}^1 q_1^3 = \mathbf{\Phi}_1^T \mathbf{f}(t) \tag{38}$$

The structure was excited with nine swept-sines from 50 to 150 Hz, and the displacement and velocity obtained at the three measurement points defined in Fig. 14a are shown in Fig. 16. This range was chosen to encompass the first linear natural frequency, which was at 91 Hz. The measured accelerations a_1 and a_3 in Fig. 14a were integrated by dividing the FFT of the signals by $i\omega$ and high-pass filtered with a butterworth filter to estimate velocity and again for displacement. The same approach was used to obtain the displacement from the laser vibrometer signal. Finally, these signals were used with the identified

mode shape matrix in Eq. (37a) to estimate q_1 and $\dot{q}_1$ in Eq. (38) as $[q_1,\ q_2]^T = \mathbf{\Phi}^{\dagger}[x_1,\ x_2,\ x_3]^{\mathrm{T}}$. Every swept-sine signal was 204.8 seconds long, and was sampled with $\Delta t = 3.9063 \times 10^{-4}$ seconds. The voltage sent to the shaker amplifier varied from 10 mV to 300 mV to activate the nonlinearity to varying degrees.

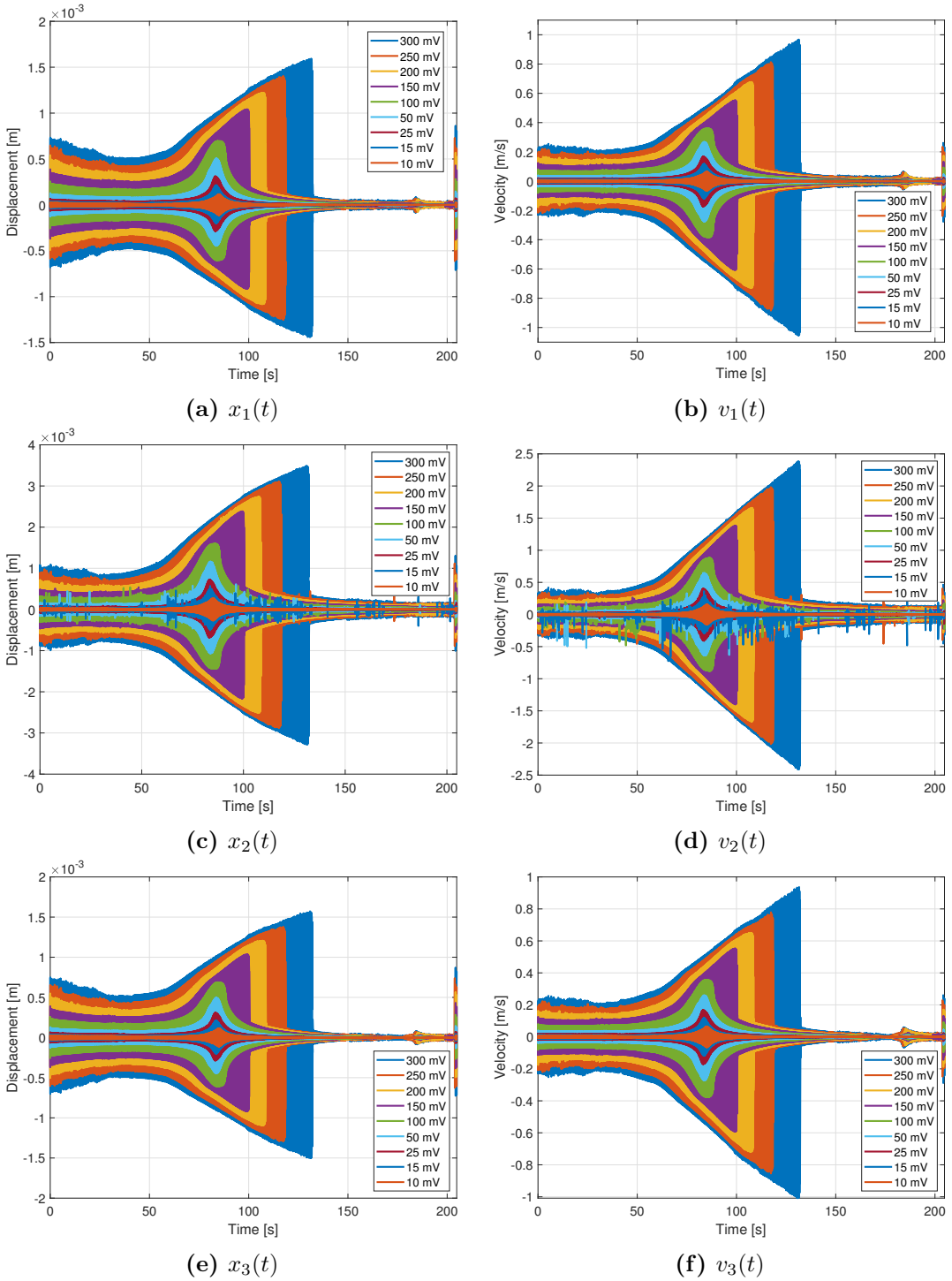

(a) $x_1(t)$ **(b)** $v_1(t)$

(c) $x_2(t)$ **(d)** $v_2(t)$

(e) $x_3(t)$ **(f)** $v_3(t)$

Fig. 16: Filtered **(a, c, e)** displacement and **(b, d, f)** velocity signals measured with the laser vibrometer and two accelerometers. Subscripts $k \in \{1, 2, 3\}$ of $x_k(t)$ and $v_k(t)$ correspond to those in Fig. 14a.

In total, the structure was excited with the swept-sines of the following amplitudes: $F_{in} \in \{10,\ 15,\ 25,\ 50,\ 100,\ 150,\ 200,\ 250,\ 300\}$ mV, or $F_{mag} \in \{1.684,\ 2.856,\ 5.199,\ 11.056,\ 22.771,\ 34.486,\ 46.201,\ 57.916,\ 69.631\} \times 10^{-3}$ N. The i/o signals collected in 7 tests were grouped into 21 pairs, listed in Tab. 14, and provided to the NIXO algorithms. These signals come from experiments where $F_{in} \in \{25,\ 50,\ 100,\ 150,\ 200,\ 250,\ 300\}$ mV; those with $F_{in} \in \{10,\ 15\}$ mV were not included because the structure was oscillating at too small of amplitudes to excite the nonlinearity significantly. To form Eqs. (12b), a 15.75-second-long Hanning windowing with an overlap of 50% was applied to each time series. This resulted in 25 spectral averages, each consisting of 20161 frequency samples. To reduce the size of the linear least squares problem, the frequency range was narrowed from (0, 1280) Hz to (50, 150) Hz (1575 frequency lines), reducing the size by a factor of 12.8.

Tab. 14: NIXO algorithms operated on pairs of input/output signals as listed below.

Voltage Amplitude $[mV]$		
1st Signal	2nd Signal	# of pairs
50	$\{\ 25\}$	1
100	$\{\ 50,\ 25\}$	2
150	$\{100,\ 50,\ 25\}$	3
200	$\{150, 100,\ 50,\ 25\}$	4
250	$\{200, 150, 100,\ 50,\ 25\}$	5
300	$\{250, 200, 150, 100,\ 50,\ 25\}$	6
	Together:	21 pairs

The identification process can be divided here into three steps: (*i*) first, NIXO was applied to all 21 pairs; then, (*ii*) the nonlinear coefficients obtained by the real and complex versions of the algorithm were compared; (*iii*) finally the nonlinear coefficients obtained were evaluated to assess their accuracy, as explained below. Those case studies that met the accuracy criteria are highlighted in green in Tab. 16 and are listed in Tab. 15. They all correspond to cases where the excitation amplitude was relatively large.

Tab. 15: The nine case studies considered to be valid.

Voltage Amplitude $[mV]$		
1st Signal	2nd Signal	# of pairs
150	$\{100\}$	1
200	$\{150, 100\}$	2
250	$\{200, 150\}$	2
300	$\{250, 200, 150, 100\}$	4
	Together:	9 pairs

Two metrics, defined in Eq. (39), were found to be helpful in identifying the cases that gave reasonable results. The γ_{real} and γ_{cmplx} parameters occurring in Eq. (39) represent the estimates of the nonlinear coefficients returned by, respectively, the real- and complex-versions of NIXO. Hence, Δ_* expresses the relative difference between the coefficient that is forced to be real and the real part of the complex one. On the other hand, Δ_{**} is defined as the relative difference between the real and imaginary parts of the complex solution.

$$\Delta_* = \frac{\|\gamma_{real} - Re\{\gamma_{cmplx}\}\|}{\gamma_{real}} \tag{39a}$$

$$\Delta_{**} = \frac{\|Re\{\gamma_{real}\} - Im\{\gamma_{cmplx}\}\|}{\|Re\{\gamma_{real}\}\|} \tag{39b}$$

NIXO was judged to have accurately identified the system when: (i) Δ_* is a small number, meaning that γ_{real} and γ_{cmplx} are similar, and (ii) Δ_{**} is close to 1.0, meaning that the imaginary part of the complex solution is relatively small. For the case studies used to date, the two consistency criteria were quantified using the tolerances shown in Eq. (40), and both were required to be satisfied simultaneously for the identification to be judged as accurate.

$$\begin{cases} \Delta_* \lesssim 0.10 \\ \Delta_{**} \gtrsim 0.90 \end{cases} \tag{40}$$

Tab. 16: Estimated values of the nonlinear coefficients obtained with the $\mathbf{D}_1$- and $\mathbf{D}_2$-based NIXO methods. Rows in which the β_{111} satisfies the consistency criteria (40) are marked with green.

$\mathbf{D}_1$-based NIXO

Case	Signal 1	Signal 2	β_{111} estimate	β_{111}^{real}	$Re\left\{\beta_{111}^{cmplx}\right\}$	$Im\left\{\beta_{111}^{cmplx}\right\}$	Δ_*	Δ_{**}
1	50	25	-1.144e+12	-1.144e+12	-1.144e+12	4.351e+12	0.00	280.23
2	100	50	4.784e+12	4.784e+12	4.784e+12	3.482e+12	0.00	27.20
3	100	25	2.996e+12	2.996e+12	2.996e+12	3.724e+12	0.00	24.28
4	150	100	1.107e+13	1.107e+13	1.107e+13	1.184e+12	0.00	89.30
5	150	50	8.032e+12	8.032e+12	8.032e+12	2.229e+12	0.00	72.25
6	150	25	6.257e+12	6.257e+12	6.257e+12	2.643e+12	0.00	57.76
7	200	150	1.320e+13	1.320e+13	1.320e+13	1.028e+12	0.00	92.21
8	200	100	1.125e+13	1.125e+13	1.125e+13	1.143e+12	0.00	89.84
9	200	50	8.832e+12	8.832e+12	8.832e+12	1.828e+12	0.00	79.30
10	200	25	7.297e+12	7.297e+12	7.297e+12	2.135e+12	0.00	70.74
11	250	200	1.620e+13	1.620e+13	1.620e+13	1.426e+12	0.00	91.20
12	250	150	1.315e+13	1.315e+13	1.315e+13	1.377e+12	0.00	89.53
13	250	100	1.125e+13	1.125e+13	1.125e+13	1.392e+12	0.00	87.63
14	250	50	8.941e+12	8.941e+12	8.941e+12	1.897e+12	0.00	78.79
15	250	25	7.575e+12	7.575e+12	7.575e+12	2.110e+12	0.00	72.14
16	300	250	1.860e+13	1.860e+13	1.860e+13	1.173e+12	0.00	93.70
17	300	200	1.564e+13	1.564e+13	1.564e+13	1.348e+12	0.00	91.38
18	300	150	1.309e+13	1.309e+13	1.309e+13	1.293e+12	0.00	90.13
19	300	100	1.140e+13	1.140e+13	1.140e+13	1.364e+12	0.00	88.03
20	300	50	9.266e+12	9.266e+12	9.266e+12	1.775e+12	0.00	80.85
21	300	25	7.992e+12	7.992e+12	7.992e+12	1.968e+12	0.00	75.38

$\mathbf{D}_2$-based NIXO

Case	Signal 1	Signal 2	β_{111} estimate	β_{111}^{real}	$Re\left\{\beta_{111}^{cmplx}\right\}$	$Im\left\{\beta_{111}^{cmplx}\right\}$	Δ_*	Δ_{**}
1	50	25	-4.624e+11	-4.624e+11	-4.624e+11	3.828e+12	0.00	727.87
2	100	50	5.306e+12	5.306e+12	5.306e+12	3.300e+12	0.00	37.81
3	100	25	3.436e+12	3.436e+12	3.436e+12	3.453e+12	0.00	0.49
4	150	100	1.093e+13	1.093e+13	1.093e+13	1.104e+12	0.00	89.90
5	150	50	7.635e+12	7.635e+12	7.635e+12	2.651e+12	0.00	65.29
6	150	25	5.826e+12	5.826e+12	5.826e+12	2.976e+12	0.00	48.93
7	200	150	1.112e+13	1.112e+13	1.112e+13	6.032e+11	0.00	94.58
8	200	100	1.043e+13	1.043e+13	1.043e+13	9.600e+11	0.00	90.80
9	200	50	8.082e+12	8.082e+12	8.082e+12	2.152e+12	0.00	73.38
10	200	25	6.605e+12	6.605e+12	6.605e+12	2.437e+12	0.00	63.10
11	250	200	1.236e+13	1.236e+13	1.236e+13	1.588e+12	0.00	87.15
12	250	150	1.093e+13	1.093e+13	1.093e+13	1.324e+12	0.00	87.88
13	250	100	1.011e+13	1.011e+13	1.011e+13	1.310e+12	0.00	87.04
14	250	50	8.242e+12	8.242e+12	8.242e+12	2.162e+12	0.00	73.77
15	250	25	6.970e+12	6.970e+12	6.970e+12	2.374e+12	0.00	65.95
16	300	250	1.322e+13	1.322e+13	1.322e+13	6.080e+11	0.00	95.40
17	300	200	1.201e+13	1.201e+13	1.201e+13	1.104e+12	0.00	90.81
18	300	150	1.094e+13	1.094e+13	1.094e+13	1.111e+12	0.00	89.85
19	300	100	1.010e+13	1.010e+13	1.010e+13	1.279e+12	0.00	87.35
20	300	50	8.491e+12	8.491e+12	8.491e+12	2.006e+12	0.00	76.37
21	300	25	7.326e+12	7.326e+12	7.326e+12	2.210e+12	0.00	69.84

5.2.2 System Identification Results

Table 16 presents the estimates of the nonlinear part of the system obtained with the $\mathbf{D}_1$- and $\mathbf{D}_2$-based NIXO methods. If one considers all of the estimates that satisfy the criteria in Eq. (40) to be independent and equally valid, then the statistics of the β_{111} parameter can be computed. The minimum and maximum observed values as well as the average and standard deviation are reported in Tab. 17.

Tab. 17: Statistical analysis of the results marked with green in Table 16.

β_{111} estimate	min	max	average	st. dev.
NIXO D1	1.11×10^{13}	1.86×10^{13}	1.37×10^{13}	17.69%
NIXO D2	1.01×10^{13}	1.32×10^{13}	1.13×10^{13}	8.28%

The true value of the nonlinear parameter β_{111} is unknown, so the NNM of the system was visualized to seek to validate these results. Figure 17 presents the NNM curves computed from Eq. (38), using various values for β_{111}, superimposed on the velocity time signals. The β_{111} values used were in the range $(1.10,\ 1.60) \times 10^{13}$ $\mathrm{kg}^{-1}\mathrm{m}^{-2}\mathrm{s}^{-2}$. Those NNMs seem to qualitatively capture the jump-down behavior of the nonlinear system, so this seems to be a reasonable range for the β_{111} parameter. Even then, the actual system seems to stiffen more slowly at first and then more rapidly at higher amplitudes, so perhaps there are additional polynomial terms that need to be added to capture the true behavior more accurately. This will be explored in future works.

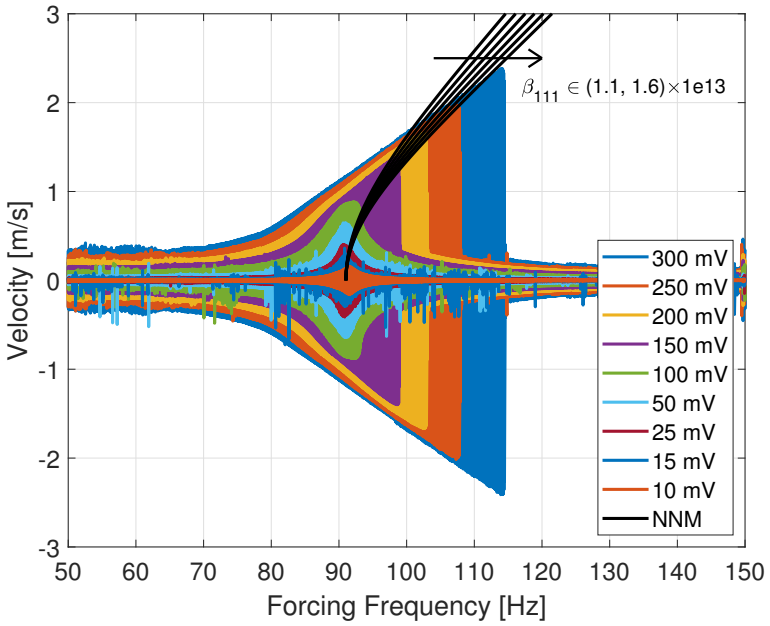

Fig. 17: The NNM curves computed from Eq. (38) and the velocity time signals measured at the beam's center.

When it comes to the linear part of the system, the linear $\mathbf{H}_1$-estimator was applied to the measured signals and (as expected) returned approximations of the linear FRFs that were distorted by the structure's nonlinearity, as shown in Fig. 18. On the other hand, Figure 19 shows the average of the frequency response functions obtained with NIXO, where the average was over those obtained from the 9 valid case studies. The reference FRF, obtained with the linear $\mathbf{H}_1$-algorithm applied to the low level data, is also shown. The nine individual results can be seen in Appendix B.

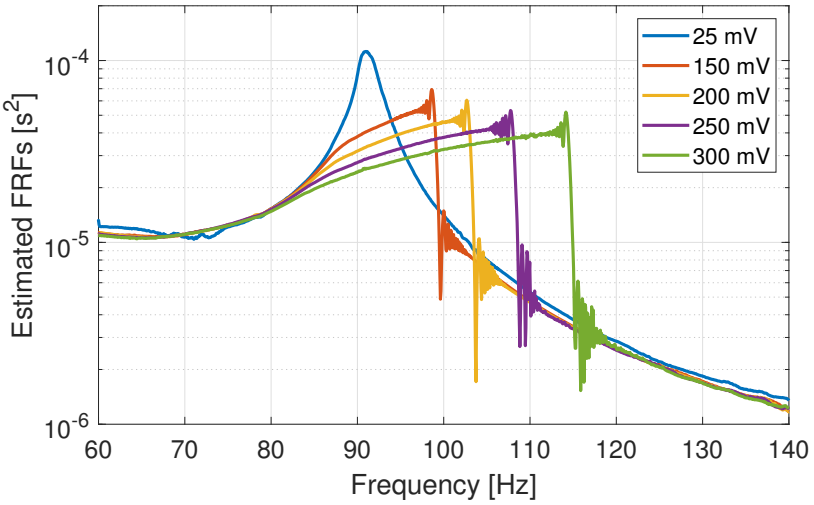

Fig. 18: The distorted FRFs returned by the linear $\mathbf{H}_1$algorithm applied to the high-level signals.

The curves displayed in Fig. 19 show that NIXO removes most of the nonlinear distortions seen in Fig. 18 from the system, capturing them with the β_{111} term. The curves are compared quantitatively in Tab. 18, as in prior sections. The relative differences between the estimated and reference natural frequencies are less than than 5.03%, while the differences between the linear damping ratios are as high as 165%.

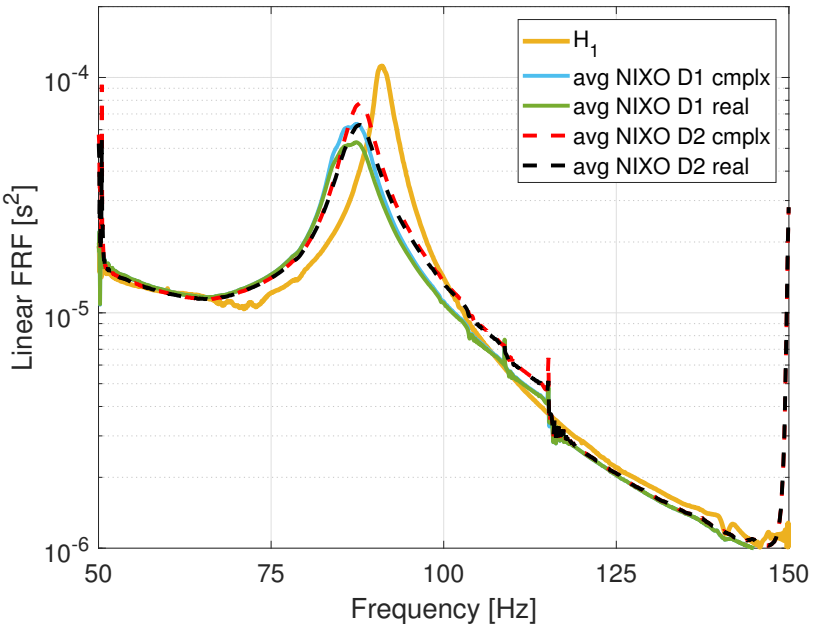

Fig. 19: Comparison of the average and reference linear FRFs.

Tab. 18: Comparison of the average and reference linear FRFs presented in Fig. 19. Relative differences are calculated with respect to the data obtained with the linear $\mathbf{H}_1$-estimator applied to the low-amplitude i/o signals.

Algorithm	nat. freq [Hz]	rel. diff.	lin. damping	rel. diff.
H1	91.076		0.0119	
NIXO D1 cmplx	86.686	(4.82%)	0.0273	(129.94%)
NIXO D1 real	86.492	(5.03%)	0.0314	(164.52%)
NIXO D2 cmplx	87.763	(3.64%)	0.0230	(94.07%)
NIXO D2 real	87.593	(3.82%)	0.0279	(135.51%)

6 Conclusion and Future Work

This paper has introduced a novel system identification method called NIXO (Nonlinear Identification through eXtended Outputs), which is an extension of NIFO (Nonlinear Identification through Feedback of the Outputs) that forces the nonlinear modal parameters to be identical at each frequency line. NIFO solves many individual linear systems of equations at each frequency sample, what implies that the calculated nonlinear parameters can vary with frequency. The NIXO algorithms return only a single value for the nonlinear modal parameters, but in turn must solve a much larger linear system of equations.

Two variations of NIXO were presented; namely, the $\mathbf{D}_1$- and $\mathbf{D}_2$-based NIXO. In the examples studied to date, both seem to give similar results and considering the fact that both can be easily applied to the same measurements, it seems advisable to try both approaches and compare the results. That said, if the measurements were known to have significantly more noise on either the input or output then one could evaluate the statistical performance of the $\mathbf{D}_1$ and $\mathbf{D}_2$ approaches and one or the other may be clearly superior.

The proposed NIXO algorithms were validated by applying them to simulated measurements from a single degree-of-freedom nonlinear system, a two-mode ICE-ROM of a flat beam and to real measurements from a 3D-printed flat beam, whose response exhibited geometric nonlinearity. The input forces used to excite the structures are either burst random or swept sine signals. In all case studies, it was observed that all algorithms gave erroneous results if the input signals used did not have large enough magnitudes. This is certainly not surprising, although what constitutes a "large enough" magnitude is not easy to define in general. In the case studies presented here, the inputs that were large enough induced an easily measurable shift in the natural frequency of the mode in question; in other words, if the linear $\mathbf{H}_1$-estimator was applied to the input and output signals it would produce an FRF that was significantly distorted. When NIXO and NIFO were successful, they removed these distortions and produced the FRF for the linearized system, i.e. the system oscillating at low amplitude.

Both NIXO and NIFO were successful in many of the case studies presented here. The algorithms are similar to some extend, i.e. analogous concepts are used in their derivation and they require almost exactly the same steps to identify a mechanical system. However, certain difference between the two methods can also be pointed out. First, the results returned by NIXO are constant and real, while those obtained with the NIFO method are frequency-dependent and complex, thus they require an additional post-processing step. Moreover, the NIFO method seems to be incompatible with the swept-sine inputs, since it produced erroneous results when such signals were used. On the other hand, NIFO works very well when the mechanical system was excited with a random forcing signal. In contrast, in all of the case studies performed to date, NIXO worked for either type of forcing signal.

Finally, while the results of the NIXO algorithm are promising to date, it did not fully capture the nonlinear dynamics of the 3D-printed, geometrically nonlinear beam. It is worth mentioning that already existing powerful methods such as PLL, CBC, and RCT have provided accurate estimates of the NNMs

geometrically nonlinear structures similar to that studied here [19, 21]. However, it is important to note that these approaches require specialized hardware to implement the closed-loop control scheme. They also typically do not identify a model that can be used to predict the response to a general input, which was the goal in this work.

Future work will further investigate the application of NIXO to structures with geometric nonlinearity, possibly by considering more complicated nonlinear models for the system, including interactions between modes. To explore the limitations of the method, NIXO should also be applied to more complex mechanical systems, such as structures with friction or material nonlinearity, or to nonlinear systems where the modes are not well-separated. Additionally, a comparison of the algorithm to effective and popular nonlinear identification methods that are currently available (such as TNSI, FNSI, or the methods using closed-loop control mentioned earlier in this section) should be conducted to determine if NIXO can identify mechanical systems that these methods can handle.

References

[1] Ginsberg, J. H., 2001. *Mechanical and Structural Vibrations: Theory and Applications.* New York: Wiley, First edition.

[2] Ewins, D. J., 2000. *Modal Testing: Theory, Practice and Application, Second Edition.* Research Studies Press LTD, Hertfordshire, Second Edition.

[3] Kerschen, G., Worden, K., Vakakis, A. F., and Golinval, J.-C., 2006. "Past, present and future of nonlinear system identification in structural dynamics". *Mechanical Systems and Signal Processing,* **20**(3), pp. 505 – 592.

[4] Noël, J., and Kerschen, G., 2017. "Nonlinear system identification in structural dynamics: 10 more years of progress". *Mechanical Systems and Signal Processing,* **83**, pp. 2 – 35.

[5] Feldman, M., 2011. *Hilbert Transform Applications in Mechanical Vibration.* John Wiley and Sons.

[6] Feldman, M., 1994. "Non-linear system vibration analysis using Hilbert transform–II. Forced vibration analysis method 'Forcevib'". *Mechanical Systems and Signal Processing,* **8**(3), pp. 309 – 318.

[7] Moldenhauer, B., Allen, M. S., and Roettgen, D., 2020. "Variation of the restoring force surface method to estimate nonlinear stiffness and damping parameters". In Proceedings of the International Conference on Noise and Vibration Engineering (ISMA), Leuven, Belgium.

[8] Iwan, W. D., 1966. "A Distributed-Element Model for Hysteresis and Its Steady-State Dynamic Response". *Journal of Applied Mechanics,* **33**(4), 12, pp. 893–900.

[9] Segalman, D. J., 2005. "A Four-Parameter Iwan Model for Lap-Type Joints". *Journal of Applied Mechanics,* **72**(5), 02, pp. 752–760.

[10] Mayes, R. L., Pacini, B. R., and Roettgen, D. R., 2016. "A Modal Model to Simulate Typical Structural Dynamic Nonlinearity". In Dynamics of Coupled Structures, Volume 4, M. Allen, R. L. Mayes, and D. Rixen, eds., Springer International Publishing, pp. 57–76.

[11] Lin, R., and Ng, T., 2018. "A new method for the accurate measurement of higher-order frequency response functions of nonlinear structural systems". *ISA Transactions,* **81**, pp. 270–285.

[12] Lin, R., and Ng, T., 2018. "Applications of higher-order frequency response functions to the detection and damage assessment of general structural systems with breathing cracks". *International Journal of Mechanical Sciences,* **148**, pp. 652–666.

[13] Schetzen, M., 1980. *The Volterra and Wiener theories of nonlinear systems.* John Wiley and Sons.

[14] Sieber, J., Gonzalez-Buelga, A., Neild, S. A., Wagg, D. J., and Krauskopf, B., 2008. "Experimental continuation of periodic orbits through a fold". *Physical Review Letters,* **100**(24), pp. 244101–1. Number: 24.

[15] Renson, L., Gonzalez-Buelga, A., Barton, D., and Neild, S., 2016. "Robust identification of backbone curves using control-based continuation". *Journal of Sound and Vibration,* **367**, pp. 145 – 158.

[16] Peter, S., and Leine, R. I., 2017. "Excitation power quantities in phase resonance testing of nonlinear systems with phase-locked-loop excitation". *Mechanical Systems and Signal Processing,* **96**, pp. 139–158.

[17] Peter, S., Scheel, M., Krack, M., and Leine, R. I., 2018. "Synthesis of nonlinear frequency responses with experimentally extracted nonlinear modes". *Mechanical Systems and Signal Processing,* **101**, pp. 498 – 515.

[18] Scheel, M., Kleyman, G., Tatar, A., Brake, M. R., Peter, S., Noël, J.-P., Allen, M. S., and Krack, M., 2020. "Experimental assessment of polynomial nonlinear state-space and nonlinear-mode models for near-resonant vibrations". *Mechanical Systems and Signal Processing,* **143**, p. 106796.

[19] Abeloos, G., Müller, F., Ferhatoglu, E., Scheel, M., Collette, C., Kerschen, G., Brake, M., Tiso, P., Renson, L., and Krack, M., 2022. "A consistency analysis of phase-locked-loop testing and control-based continuation for a geometrically nonlinear frictional system". *Mechanical Systems and Signal Processing,* **170**, p. 108820.

[20] Karaağaçlı, T., and Özgüven, H. N., 2021. "Experimental modal analysis of nonlinear systems by using response-controlled stepped-sine testing". *Mechanical Systems and Signal Processing,* **146**, p. 107023.

[21] Karaağaçlı, T., and Özgüven, H. N., 2022. "Experimental Quantification and Validation of Modal Properties of Geometrically Nonlinear Structures by Using Response-Controlled Stepped-Sine Testing". *Experimental Mechanics,* **62**(2), Feb., pp. 199–211.

[22] Kwarta, M., and Allen, M. S., 2022. "Nonlinear Normal Mode backbone estimation with near-resonant steady state inputs". *Mechanical Systems and Signal Processing,* **162**, p. 108046.

[23] Masri, S. F., and Caughey, T. K., 1979. "A Nonparametric Identification Technique for Nonlinear Dynamic Problems". *Journal of Applied Mechanics,* **46**(2), 06, pp. 433–447.

[24] Bonisoli, E., and Vigliani, A., 2007. "Identification techniques applied to a passive elasto-magnetic suspension". *Mechanical Systems and Signal Processing,* **21**(3), pp. 1479 – 1488.

[25] Göge, D., and Sinapius, J. M., 2006. "Experiences with dynamic load simulation by means of modal forces in the presence of structural non-linearities". *Aerospace Science and Technology,* **10**(5), pp. 411 – 419.

[26] Aykan, M., and Özgüven, H. N., 2013. "Identification of restoring force surfaces in nonlinear mdof systemsfrom frf data using nonlinearity matrix". In Topics in Nonlinear Dynamics, Volume 1, G. Kerschen, D. Adams, and A. Carrella, eds., Springer New York, pp. 65–76.

[27] Moldenhauer, B., Roettgen, D. R., and Pacini, B., 2021. "Implementing the Restoring Force Surface Method to Fit Experimentally Measured Modal Coupling Effects". In Nonlinear Structures & Systems, Volume 1, G. Kerschen, M. R. Brake, and L. Renson, eds., Springer International Publishing, pp. 79–82.

[28] Chen, Q., Worden, K., Peng, P., and Leung, A., 2007. "Genetic algorithm with an improved fitness function for (N)ARX modelling". *Mechanical Systems and Signal Processing,* **21**(2), pp. 994 – 1007.

[29] Peng, Z., Lang, Z., Wolters, C., Billings, S., and Worden, K., 2011. "Feasibility study of structural damage detection using NARMAX modelling and Nonlinear Output Frequency Response Function based analysis". *Mechanical Systems and Signal Processing,* **25**(3), pp. 1045 – 1061.

[30] Lacy, S., and Bernstein, D., 2005. "Subspace identification of nonlinear systems with measured-input nonlinearities". *International Journal of Control,* **78**, 08, pp. 906–926.

[31] Marchesiello, S., and Garibaldi, L., 2008. "A time domain approach for identifying nonlinear vibrating structures by subspace methods". *Mechanical Systems and Signal Processing,* **22**(1), pp. 81–101.

[32] Richards, C., and Singh, R., 1998. "Identification of multi-degree-of-freedom non-linear systems under random excitations by the "reverse path" spectral method". *Journal of Sound and Vibration,* **213**(4), pp. 673 – 708.

[33] Adams, D., and Allemang, R., 2000. "A Frequency Domain Method for Estimating the Parameters of a Non-Linear Structural Dynamic Model Through Feedback". *Mechanical Systems and Signal Processing,* **14**(4), pp. 637 – 656.

[34] Haroon, M., and Adams, D. E., 2009. "A modified H_2 algorithm for improved frequency response function and nonlinear parameter estimation". *Journal of Sound and Vibration,* **320**, 03, pp. 822–837.

[35] Magnevall, M., Josefsson, A., Ahlin, K., and Broman, G., 2012. "Nonlinear structural identification by the "reverse path" spectral method". *Journal of Sound and Vibration,* **331**(4), pp. 938 – 946.

[36] Noël, J., and Kerschen, G., 2013. "Frequency-domain subspace identification for nonlinear mechanical systems". *Mechanical Systems and Signal Processing,* **40**(2), pp. 701–717.

[37] Spottswood, S., and Allemang, R., 2006. "Identification of nonlinear parameters for reduced order models". *Journal of Sound and Vibration,* **295**(1), pp. 226 – 245.

[38] Piombino, D., Allen, M. S., Ehrhardt, D., Beberniss, T., and Hollkamp, J. J., 2019. "System identification to estimate the nonlinear modes of a gong". In Nonlinear Dynamics, Volume 1, G. Kerschen, ed., Springer International Publishing, pp. 121–136.

[39] Hollkamp, J. J., Gordon, R. W., and Spottswood, S. M., 2005. "Nonlinear modal models for sonic fatigue response prediction: a comparison of methods". *Journal of Sound and Vibration,* **284**(3), pp. 1145 – 1163.

[40] Hollkamp, J. J., and Gordon, R. W., 2008. "Reduced-order models for nonlinear response prediction: Implicit condensation and expansion". *Journal of Sound and Vibration,* **318**(4), pp. 1139–1153.

[41] Park, K., and Allen, M. S., 2021. "Quasi-static modal analysis for reduced order modeling of geometrically nonlinear structures". *Journal of Sound and Vibration,* **502**, p. 116076.

[42] Safari, S., and Londono Monsalve, J., 2021. "Nonlinear function selection and parameter estimation of structures with localised nonlinearities, part 1: Numerical analysis". In Nonlinear Structures & Systems, Volume 1, G. Kerschen, M. R. Brake, and L. Renson, eds., Springer International Publishing, pp. 139–149.

[43] Safari, S., and Londono Monsalve, J., 2021. "Benchmarking optimisation methods for model selection and parameter estimation of nonlinear systems". *Vibration,* **4**(3), pp. 648–665.

[44] Kwarta, M., and Allen, M. S., 2022. "Nonlinear Identification through eXtended Outputs with Numerical and Experimental Validation using Geometrically Nonlinear Structures (Extended Version)". Available at: `https://byusdrg.com/publications/` (unpublished). Tech. rep.

[45] Napolitano, K. L., 2016. "Using singular value decomposition to estimate frequency response functions". In Topics in Modal Analysis & Testing, Volume 10, M. Mains, ed., Springer International Publishing, pp. 27–43.

[46] Rosenberg, R. M., 1960. "Normal Modes of Nonlinear Dual-Mode Systems". *Journal of Applied Mechanics,* **27**, pp. 263 – 268.

[47] Rosenberg, R. M., 1961. "On Normal Vibrations of a General Class of Nonlinear Dual-Mode Systems". *Journal of Applied Mechanics,* **28**, pp. 275 – 283.

[48] Rosenberg, R. M., 1962. "The Normal Modes of Nonlinear n-Degree-of-Freedom Systems". *Journal of Applied Mechanics,* **29**(1), 03, pp. 7–14.

[49] Rosenberg, R. M., 1966. "On Nonlinear Vibrations of Systems with Many Degrees of Freedom". *Advances in Applied Mechanics,* **9**, pp. 155 – 242.

[50] King, M. E., and Vakakis, A. F., 1994. "An Energy-Based Formulation for Computing Nonlinear Normal Modes in Undamped Continuous Systems". *Journal of Vibration and Acoustics,* **116**(3), 07, pp. 332–340.

[51] Vakakis, A. F., Manevitch, L. I., Mikhlin, Y. V., Pilipchuk, V. N., and Zevin, A. A., 1996. *Normal Modes and Localization in Nonlinear Systems.* Wiley.

[52] Vakakis, A. F., 1997. "Non-Linear Normal Modes (NNMs) and Their Applications in Vibration Theory: An Overview". *Mechanical Systems and Signal Processing,* **11**(1), pp. 3 – 22.

[53] Peeters, M., Viguié, R., Sérandour, G., Kerschen, G., and Golinval, J.-C., 2009. "Nonlinear normal modes, part ii: Toward a practical computation using numerical continuation techniques". *Mechanical Systems and Signal Processing,* **23**(1), pp. 195 – 216. Special Issue: Non-linear Structural Dynamics.

[54] Ramlan, R., Brennan, M. J., Kovacic, I., Mace, B. R., and Burrow, S. G., 2016. "Exploiting knowledge of jump-up and jump-down frequencies to determine the parameters of a duffing oscillator". *Communications in Nonlinear Science and Numerical Simulation,* **37**, pp. 282 – 291.

[55] Allen, M. S., and Ginsberg, J. H., 2006. "A global, single-input–multi-output (SIMO) implementation of the algorithm of mode isolation and application to analytical and experimental data". *Mechanical Systems and Signal Processing,* **20**(5).

[56] Vakakis, A. F., McFarland, D. M., Bergman, L., Manevitch, L. I., and Gendelman, O., 2004. "Isolated Resonance Captures and Resonance Capture Cascades Leading to Single- or Multi-Mode Passive Energy Pumping in Damped Coupled Oscillators". *Journal of Vibration and Acoustics,* **126**(2), 05, pp. 235–244.

[57] Kerschen, G., Lee, Y. S., Vakakis, A. F., McFarland, D. M., and Bergman, L. A., 2005. "Irreversible passive energy transfer in coupled oscillators with essential nonlinearity". *SIAM Journal on Applied Mathematics,* **66**(2), pp. 648–679.

[58] Kwarta, M., and Allen, M. S., 2021. "Extensions to NIFO and CRP to Estimate Frequency-Independent Nonlinear Parameters". In Special Topics in Structural Dynamics & Experimental Techniques, Volume 5, D. S. Epp, ed., Springer International Publishing, pp. 99–119.

[59] Hollkamp, J., Gordon, R., and Spottswood, S., 2003. "Nonlinear sonic fatigue response prediction from finite element modal models: A comparison with experiments". In 44th AIAA/ASME/ASCE/AHS/ASC Structures, Structural Dynamics, and Materials Conference.

[60] Tomlinson, G., 1979. "Force distortion in resonance testing of structures with electro-dynamic vibration exciters". *Journal of Sound and Vibration,* **63**(3), pp. 337–350.

Appendices

A NIFO Algorithms for Reduced Order Models

A.1 $\mathbf{H}_1$–based NIFO for ROMs

The original NIFO estimator was proposed in [33]. It is derived by first rearranging Eq. (12b) into the form presented in (B1a) and then post-multiplying the equation by matrix $\begin{bmatrix}\boldsymbol{\Psi}_k^H & (\mathbf{P}_1^v)^H & \dots & (\mathbf{P}_1)^H & \dots\end{bmatrix}$, vide Eq. (B1b). The modified $\mathbf{H}_1$ algorithm is based on Eq. (B2), where the quantity H stands for the Frequency Response Function (FRF) defined in Eq. (11). Note that Eq. (B2) can be written and solved separately for each individual frequency sample.

$$\mathbf{Q}_k = \begin{bmatrix} H_k & -\gamma_1^v H_k & \dots & -\gamma_1 H_k & \dots \end{bmatrix} \begin{bmatrix} \boldsymbol{\Psi}_k \\ \mathbf{P}_1^v \\ \vdots \\ \mathbf{P}_1 \\ \vdots \end{bmatrix} \tag{B1a}$$

$$\begin{aligned} &\mathbf{Q}_k \begin{bmatrix}\boldsymbol{\Psi}_k^H & (\mathbf{P}_1^v)^H & \dots & (\mathbf{P}_1)^H & \dots\end{bmatrix} = \\ &= \begin{bmatrix} H_k & -\gamma_1^v H_k & \dots & -\gamma_1 H_k & \dots \end{bmatrix} \begin{bmatrix} \boldsymbol{\Psi}_k \\ \mathbf{P}_1^v \\ \vdots \\ \mathbf{P}_1 \\ \vdots \end{bmatrix} \begin{bmatrix}\boldsymbol{\Psi}_k^H & (\mathbf{P}_1^v)^H & \dots & (\mathbf{P}_1)^H & \dots\end{bmatrix} \end{aligned} \tag{B1b}$$

$$\underbrace{\begin{bmatrix} S_{Q\Psi} & S_{QP_1^v} & \dots & S_{QP_1} & \dots \end{bmatrix}}_{\mathbf{S}_{H1}^{cross}} = \underbrace{\begin{bmatrix} H_k & \gamma_1^v H_k \dots & \gamma_1 H_k & \dots \end{bmatrix}}_{\mathbf{x}} \underbrace{\begin{bmatrix} S_{\Psi\Psi} & S_{\Psi P_1^v} & \dots & S_{\Psi P_1} & \dots \\ & S_{P_1^v P_1^v} & \dots & S_{P_1^v P_1} & \dots \\ & & \ddots & & \ddots \\ & & & S_{P_1 P_1} & \dots \\ & & & & \ddots \end{bmatrix}}_{\mathbf{S}_{H1}^{auto}} \tag{B2}$$

The Hermitian Matrix

The $\mathbf{H}_1$–based NIFO algorithm results in multiple systems of linear equations of a form $\mathbf{S}_{H1}^{cross} = \mathbf{x}\mathbf{S}_{H1}^{auto}$. Matrix $\mathbf{S}_{H1}^{auto}$ is square and – for the structural dynamics problems considered in this work – it is usually non-singular. Hence, it might be possible to accurately estimate the frequency response function $H(\Omega)$ and parameters γ_j^v and γ_j via solving Eq. (B2). It is worth mentioning that these linear problems are of much smaller size than their NIXO-counterparts. However, NIFO requires solving multiple systems (each corresponding to a different frequency line), while the focus of NIXO is solving only one *relatively large* linear problem.

Note that the nonlinear parameters γ_j^v and γ_j are introduced in Eq. (7) as *real* and *constant* numbers. However, if the Eq. (B2) is solved, they will be found as *complex* and possibly *frequency-dependent*, since (as already mentioned above) some of the parameters in Eq. (B2) are complex and the system of equations is solved for each individual frequency sample.

A.2 $\mathbf{H}_2$–based NIFO for ROMs

The $\mathbf{H}_2$–based NIFO algorithm was first presented in [34]. Its derivation starts with extending Eq. (B1a) with additional pseudo-outputs. They correspond to the nonlinear terms in the EOM, as shown in Eq. (B3a). Then, in order to obtain Eq. (B4), which is the base formula of the modified $\mathbf{H}_2$ algorithm, one must right-multiply Eq. (B3a) by matrix $\begin{bmatrix}\mathbf{Q}^H & (\mathbf{P}_1^{v,k})^H & \dots & (\mathbf{P}_1^{k})^H & \dots\end{bmatrix}$, see Eq. (B3b).

$$\begin{bmatrix}\mathbf{Q}_k\\ \mathbf{P}_1^{v,k}\\ \vdots\\ \mathbf{P}_1^{k}\\ \vdots\end{bmatrix} = \begin{bmatrix}H_k & -\gamma_1^v H_k & \dots & -\gamma_1 H_k & \dots\\ & 1 & & & \\ & & \ddots & & \\ & & & 1 & \\ & & & & \ddots\end{bmatrix}\begin{bmatrix}\mathbf{\Psi}_k\\ \mathbf{P}_1^{v,k}\\ \vdots\\ \mathbf{P}_1^{k}\\ \vdots\end{bmatrix} \tag{B3a}$$

$$\begin{bmatrix}\mathbf{Q}_k\\ \mathbf{P}_1^{v,k}\\ \vdots\\ \mathbf{P}_1^{k}\\ \vdots\end{bmatrix}\begin{bmatrix}\mathbf{Q}^H & (\mathbf{P}_1^{v,k})^H & \dots & (\mathbf{P}_1^{k})^H & \dots\end{bmatrix} =$$

$$\begin{bmatrix}H_k & -\gamma_1^v H_k & \dots & -\gamma_1 H_k & \dots\\ & 1 & & & \\ & & \ddots & & \\ & & & 1 & \\ & & & & \ddots\end{bmatrix}\begin{bmatrix}\mathbf{\Psi}_k\\ \mathbf{P}_1^{v,k}\\ \vdots\\ \mathbf{P}_1^{k}\\ \vdots\end{bmatrix}\begin{bmatrix}\mathbf{Q}^H & (\mathbf{P}_1^{v,k})^H & \dots & (\mathbf{P}_1^{k})^H & \dots\end{bmatrix} \tag{B3b}$$

$$\overbrace{\begin{bmatrix}S_{QQ} & S_{QP_1^v} & \dots & S_{QP_1} & \dots\\ & S_{P_1^vP_1^v} & \dots & S_{P_1^vP_1} & \dots\\ & & \ddots & & \ddots\\ & \textbf{Hermitian Matrix} & & S_{P_1P_1} & \dots\\ & & & & \ddots\end{bmatrix}}^{\mathbf{S}_{H2}^{auto}} =$$

$$= \underbrace{\begin{bmatrix}H_k & -\gamma_1^v H_k & \dots & -\gamma_1 H_k & \dots\\ & 1 & & & \\ & & \ddots & & \\ & & & 1 & \\ & & & & \ddots\end{bmatrix}}_{\mathbf{X}}\underbrace{\begin{bmatrix}S_{\Psi Q} & S_{\Psi P_1^v} & \dots & S_{\Psi P_1} & \dots\\ S_{P_1^vQ} & S_{P_1^vP_1^v} & \dots & S_{P_1^vP_1} & \dots\\ \vdots & \textbf{Herm. Sub-mtrx} & & \ddots & \ddots\\ S_{P_1Q} & & & S_{P_1P_1} & \dots\\ \vdots & & & & \ddots\end{bmatrix}}_{\mathbf{S}_{H2}^{cross}} \tag{B4}$$

Analogous to the $\mathbf{H}_1$–based NIFO, its $\mathbf{H}_2$-based twin also estimates the nonlinear γ_j^v- and γ_j-parameters as complex and frequency-dependent. A detailed derivation of the method together with the case studies illustrating its accuracy and performance are presented in [34].

B Linear FRFs From the Nine Valid Experimental Case Studies

Figure 20 presents the linear frequency response functions found by NIXO in the nine case studies marked with green in Tab 16. In these system identification attempts only, the Δ-parameters – specified in Eq. (39) – satisfy the accuracy criteria (40). Additionally, the FRF curves are compared to the reference ones obtained with the popular linear $\mathbf{H}_1$-estimator applied to the low-amplitude i/o signals. The results presented in the nine subplots below were used to calculate the average linear FRF presented in Fig. 19

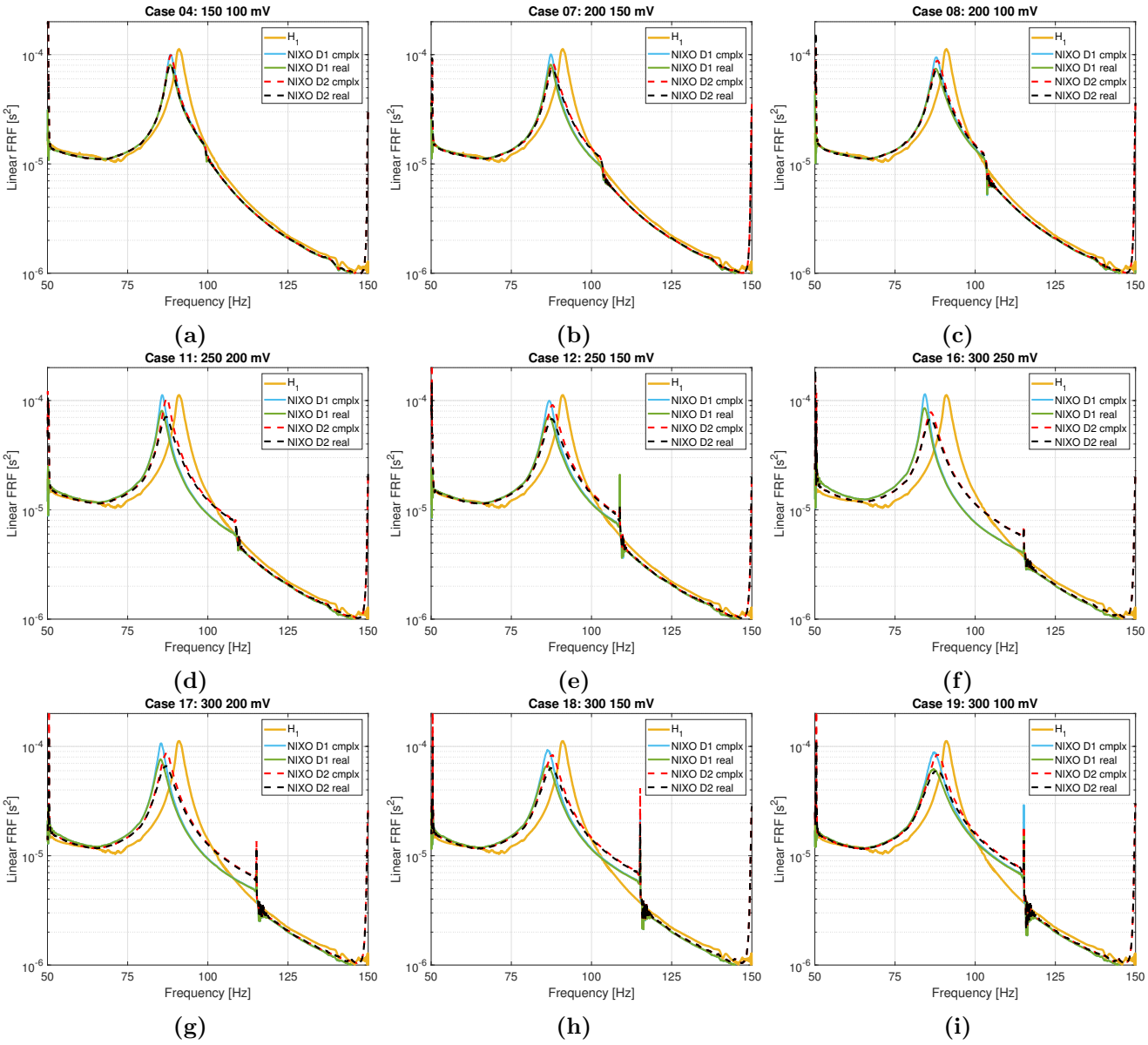

Fig. 20: Linear FRFs found in the case studies marked with green in Tab. 16.